



**HAL**  
open science

## Moon meteoritic seismic hum: Steady state prediction

Philippe Lognonné, Mathieu Le Feuvre, Catherine L. Johnson, Renee Weber

► **To cite this version:**

Philippe Lognonné, Mathieu Le Feuvre, Catherine L. Johnson, Renee Weber. Moon meteoritic seismic hum: Steady state prediction. *Journal of Geophysical Research*, 2009, 114 (E12), pp.IPGP contribution 2540. 10.1029/2008JE003294 . insu-02567454

**HAL Id: insu-02567454**

**<https://insu.hal.science/insu-02567454>**

Submitted on 26 May 2020

**HAL** is a multi-disciplinary open access archive for the deposit and dissemination of scientific research documents, whether they are published or not. The documents may come from teaching and research institutions in France or abroad, or from public or private research centers.

L'archive ouverte pluridisciplinaire **HAL**, est destinée au dépôt et à la diffusion de documents scientifiques de niveau recherche, publiés ou non, émanant des établissements d'enseignement et de recherche français ou étrangers, des laboratoires publics ou privés.

## Moon meteoritic seismic hum: Steady state prediction

Philippe Lognonné,<sup>1</sup> Mathieu Le Feuvre,<sup>1</sup> Catherine L. Johnson,<sup>2</sup> and Renee C. Weber<sup>3</sup>

Received 8 November 2008; revised 10 July 2009; accepted 17 August 2009; published 23 December 2009.

[1] We use three different statistical models describing the frequency of meteoroid impacts on Earth to estimate the seismic background noise due to impacts on the lunar surface. Because of diffraction, seismic events on the Moon are typically characterized by long codas, lasting 1 h or more. We find that the small but frequent impacts generate seismic signals whose codas overlap in time, resulting in a permanent seismic noise that we term the “lunar hum” by analogy with the Earth’s continuous seismic background seismic hum. We find that the Apollo era impact detection rates and amplitudes are well explained by a model that parameterizes (1) the net seismic impulse due to the impactor and resulting ejecta and (2) the effects of diffraction and attenuation. The formulation permits the calculation of a composite waveform at any point on the Moon due to simulated impacts at any epicentral distance. The root-mean-square amplitude of this waveform yields a background noise level that is about 100 times lower than the resolution of the Apollo long-period seismometers. At 2 s periods, this noise level is more than 1000 times lower than the low noise model prediction for Earth’s microseismic noise. Sufficiently sensitive seismometers will allow the future detection of several impacts per day at body wave frequencies.

**Citation:** Lognonné, P., M. Le Feuvre, C. L. Johnson, and R. C. Weber (2009), Moon meteoritic seismic hum: Steady state prediction, *J. Geophys. Res.*, *114*, E12003, doi:10.1029/2008JE003294.

### 1. Introduction

[2] During the nearly eight years of operation of the Apollo seismic network, approximately 1700 meteoroid impacts were detected on the long-period seismometers. The most recent event catalog, updated by Y. Nakamura in October 2008 and available online from the University of Texas (<ftp://ftp.ig.utexas.edu/pub/PSE/catsrepts/>) reports 1010 impacts recorded at the Apollo 12 landing site. This leads to a detection rate of 128 events per year at that station, less than the deep moonquake rate of about 465 per year. Meteoroid impacts on the Moon are interesting and important sources for seismic experiments that might be deployed in the next decade, under the framework of new initiatives such as the International Moon Exploration program (including the NASA/ILN, JAXA/SELENE2, RKA/LUNARGLOB and other ESA, Indian and Chinese projects). These events occur at the surface and so only the time and geographical position are needed to characterize their source locations and to use them for travel time inversions, making studies on the crustal thickness possible [e.g., *Chenet et al.*, 2006]. During the Apollo lander missions, impacts with well-known locations and times were limited to the artificial impacts of the upper

stage of Saturn V rocket (the SIVB) and of the Lunar Module (LM). More recently, it has been shown that the time and geographical location of impacting meteoroids can be obtained by monitoring light emissions generated during the impact [*Ortiz et al.*, 2006], which provides new opportunities for modeling the arrival times of seismic waves from these events.

[3] In this paper, we provide an estimate of the background seismic noise due to meteorites impacting the Moon, giving our result as the minimum value of the root-mean-square (rms) surface acceleration. This background noise was not recorded by the Apollo seismic experiment despite a seismometer resolution of  $0.5 \times 10^{-10}$  m at a period of 2 s. Due to diffraction processes, a single seismic event has a typical duration of 1 h or more. Thus frequent small impacts, distributed globally, and impacting the Moon at hourly intervals or less, will generate signals that overlap in time. A continuous background seismic noise results, that despite the different excitation process and different frequency band of the signal, can be seen as analogous to the Earth’s seismic hum [e.g., *Kobayashi and Nishida*, 1998; *Webb*, 2008]. We term this continuous background noise the lunar hum.

[4] Our approach is similar to those of *Laster and Press* [1968] and *McGarr et al.* [1969], who, prior to the Apollo missions, predicted the level of meteorite detection as a function of the lunar attenuation properties. In contrast to these earlier studies, we are now able to test predictions using the Apollo seismic data. However, in order to detect the lunar hum in the future (and more fully explore the seismicity of the Moon), the estimation of its amplitude will be a major specification in the design of a new generation of lunar seismometers. Such detection will also allow a better assess-

<sup>1</sup>Equipe Géophysique Spatiale et Planétaire, UMR 7154, Institut de Physique du Globe de Paris, Université Paris Diderot, CNRS, Saint Maur des Fosses, France.

<sup>2</sup>Department of Earth and Ocean Sciences, University of British Columbia, Vancouver, British Columbia, Canada.

<sup>3</sup>U.S. Geological Survey, Flagstaff, Arizona, USA.

ment of more ambitious goals in lunar seismology, such as the recently proposed detection of strange quark matter impacts [Banerdt *et al.*, 2006]. Finally, future recording of lunar seismic noise may allow new types of investigations of lunar interior structure, such as recent tomographic studies performed on the Earth using the continuous microseismic noise [Shapiro and Campillo, 2004; Shapiro *et al.*, 2005], and inversions for very shallow regolith structure on the Moon using high-frequency thermally induced noise [Larose *et al.*, 2005; Tanimoto *et al.*, 2008].

[5] We estimate the meteoritic seismic background noise on the Moon as follows: (1) We review how impacts generate seismic signals and use the artificial lunar impacts to calibrate the relationship between impactor parameters and the seismic data amplitudes. (2) We compute synthetic seismic waveforms generated by impacts with a given impact mass and velocity at any epicentral distance, using the calibration calculated in the first step. (3) We then use three different meteoroid mass/frequency laws to generate, with a random simulator, a history of impacts on the Moon during a given time interval. (4) We compute the cumulative seismic signal generated by a succession of impacts and use this signal to calculate the seismic background noise at a given location. We conclude by discussing our results and providing an estimate of the seismic background noise and some constraints on the attenuation of the deep lunar interior.

## 2. Background: Impacts on the Moon

[6] The four Apollo seismometers operating in network mode were extremely sensitive, capable of detecting displacements of  $3 \times 10^{-10}$  m at frequencies between 0.1 and 1 Hz on the long-period (LP) instrument in flat response mode,  $0.5 \times 10^{-10}$  m at 0.45 Hz for the LP instrument in peaked response mode, and  $0.5 \times 10^{-10}$  m at 8 Hz for the short-period (SP) instrument [Lammlein *et al.*, 1974]. This led to the detection of over 12,500 seismic signals (see Nakamura *et al.* [1981] for catalog) between July 1969 and September 1977; many more events that were recorded only on the SP channels remain uncataloged. Despite their sensitivity, the Apollo instruments were unable to detect any continuous microseismic noise, and recorded significant background noise only around the times of sunrise and sunset, due to thermal effects in the shallow subsurface.

[7] About 1700 of the events listed in the catalog are meteorite impacts. These events have been studied in detail by Oberst and Nakamura [1987a, 1987b, 1991], who found that 28% of small events (impactors which were detected at only one station and are therefore likely to have small masses) were associated with showers, including ones of cometary origin. Large events were found to be less frequently associated with showers (15%).

[8] In order to separate the events specifically associated with showers from the background population of impactors, we computed amplitude/frequency distributions for three groups of impact events (Figure 1), using the compressed-scale envelope amplitudes listed in the catalog (for a description of how these amplitudes were computed, see Nakamura *et al.* [1980]). Note that the detection of impacts is compared to the detection of deep moonquakes (green and blue curves); this will be discussed in more detail in the last chapter of this section.

[9] The first group consists of all impacts detected by Apollo 12 between Julian day 1 of 1970 (1970/001) and Julian day 288 of 1974 (1974/288), a period during which the Apollo 12 seismic station was operated in peaked response mode (we differentiate between events recorded in peaked response and flat response modes since they have different transfer functions and hence generate amplitudes that are not directly comparable) [see, e.g., Bulow *et al.*, 2005]. The second group consists of events from the same period, but excludes events associated with the 13 shower periods compiled by Oberst and Nakamura [1991]. Out of a total of 1749 days, this leads to the exclusion of 857 days (see Oberst and Nakamura [1991, Table 2] for meteoroid shower times). The last group is for the 857 days during shower periods. As seen in Figure 1, excluding events associated with showers slightly modifies the amplitude/frequency curve. The resulting impact rates are 125, 192, 130, and 170 events per year at stations 12, 14, 15, and 16 respectively. The main difference between the distributions during and outside the shower period is a slight increase during shower periods in the number of events with amplitudes reaching a few mm in compressed scale. However, this difference is statistically not well constrained, as shown by the error bars in Figure 1. In this paper we use the frequency distribution at times excluding showers.

[10] We now compare the amplitude of impacts at the different Apollo stations. The compressed-scale envelope amplitudes listed in the catalog are not consistent among stations: the Z component was used for station 12 amplitudes, while the Y component was used for stations 14, 15, and 16. To compare the amplitude/frequency distributions at different stations, we estimated amplitudes directly from the Apollo waveforms. These are shown in Figure 2, using the maximum peak-to-peak amplitude in Apollo digital units ( $1 \text{ DU} = 0.5 \times 10^{-10}$  m in ground displacement at a period of 2 s) of each impact seismogram after despiking [Evans, 1982]. The despiking algorithm used prior to amplitude calculation [see Bulow *et al.*, 2005] may partially account for bit errors during transmission, but not for the bit error related to the Apollo 14 electronic malfunction. We thus discuss only the amplitudes recorded at Apollo stations 12, 15 and 16. We see differences in terms of detection efficiency for the vertical and horizontal components. For example, we see that the amplitudes of events detected at station 12 on the long-period X-Y components are smaller than those at Apollo 16. This effect is likely related to the preferential amplification of energy along different axes due to site effects associated with the regolith [Lammlein *et al.*, 1974; Toksoz *et al.*, 1977]. In Figure 3 we show the relationship between the Z and X amplitudes at stations 12, 15 and 16. Amplitudes on both station 12 components are comparable; this is not the case for the other stations, as larger amplitudes are generally found on the X component of stations 15 and 16. We thus focus our study on the LP vertical component of the Apollo 12 station.

[11] We note that deep moonquake activity typically generates three times more small events than impact activity. We have plotted on Figure 1 the detection statistics for two different time periods. The first period is when the distance between the Earth and Moon is closer to the mean distance (green points on Figure 1), while the second period is when the Earth-Moon distance is closer to its extreme values (blue

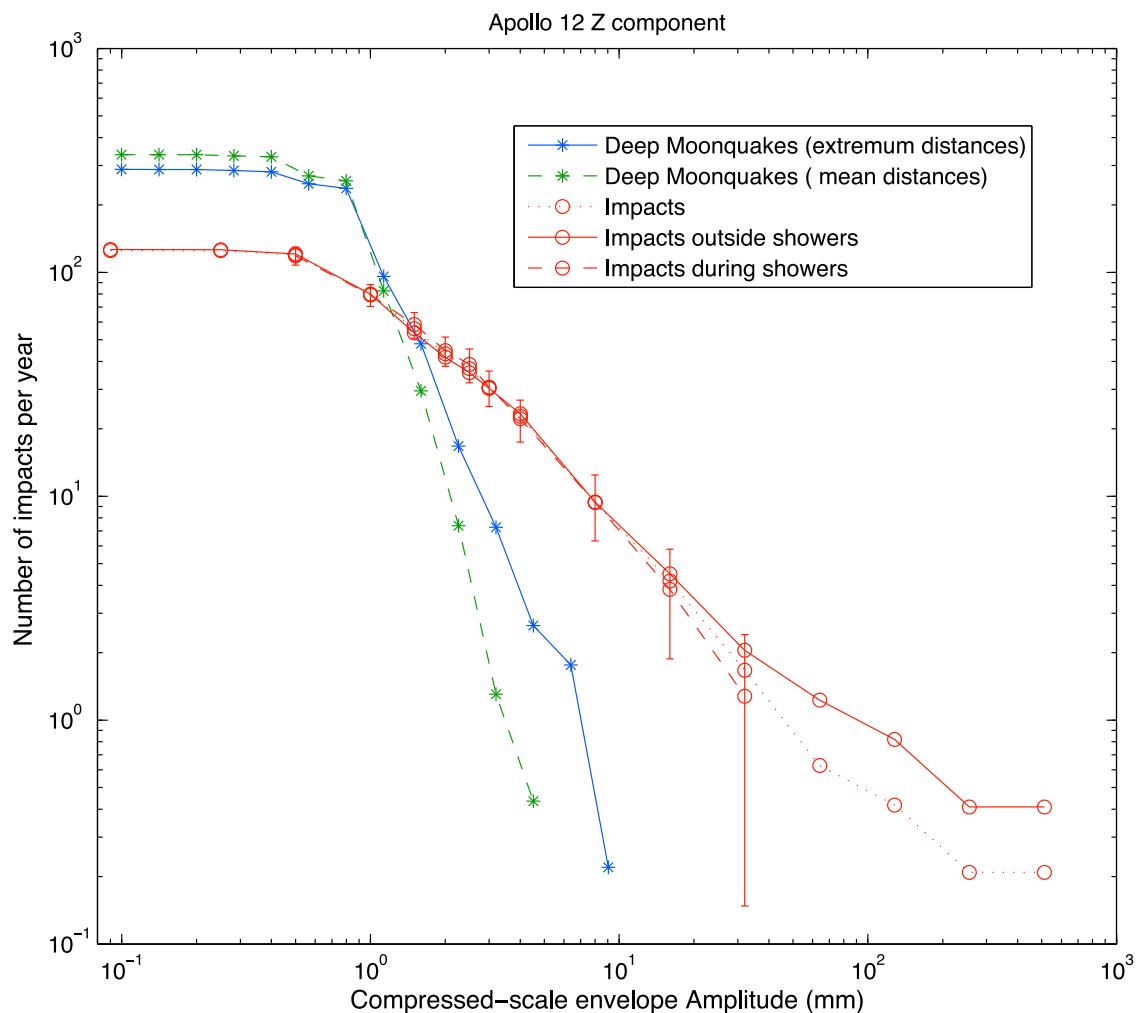


**Figure 1.** Number of impacts per year with a given compressed-scale envelope amplitude in log-log scale. The impact list at station 12 is given by *Nakamura et al.* [1981] (for a current version see <ftp://ftp.ig.utexas.edu/pub/PSE/catsrepts/>). The dotted red curve is for all impacts between 1970/001 and 1974/288, while the solid and dashed red curves are for the periods outside and during showers, respectively. All large events occurred during the nonshower periods, which explains why the curve for the shower period stops at amplitudes of 30 mm. The only significant difference between the shower and nonshower curves is the slight amplification of small events with amplitudes around 3 mm in compressed scale. In all cases, the number of events are normalized to a 1 year period (see text for details). The error (defined as the square root of the number of events) is given for only one curve but is similar for all curves. For comparison, the amplitude/number distribution for deep moonquakes is shown in green and blue during the same period. Green points show the statistics when the distance between the Earth and Moon is within 50% of its maximum excursion from the mean distance, while the blue points are those when the distance is between 50% and 100% of its maximum excursion from the mean distance.

points on Figure 1). Figures 4a and 4b show the individual events used for these statistics. We see that large events occur preferentially when the Moon reaches extreme distances, as denoted by the slope differences in the statistics on Figure 1. The mean number of small quakes in both cases is similar, on the order of 300 events per year. This activity of small events is strongly time-dependent, as the deep moonquakes are known to be triggered by the Earth's tides on the Moon [e.g., *Lammlein et al.*, 1974; *Frohlich and Nakamura*, 2009]. A significant periodicity is therefore observed in the deep moonquake activity [*Ewing et al.*, 1971], as shown on Figure 4c. The number of quakes in a 2 week period varies

from about 10 to more than 40. Cyclic variations are found also in the mean amplitude of the moonquakes, even for the smallest 50% of quakes (Figure 4d), with variations of about 0.5 mm in compressed scale up to 1.5 mm or more. Finally, a reduction of the number-amplitude slope for small amplitude events is found not only at station 12 (Figure 1), but also on stations 14 and 16, where the amplitudes are larger (see above or see *Frohlich and Nakamura* [2009, Figure 7] for the deep moonquakes). The slope reduction is thus likely related to a real limit on small deep moonquake activity, rather than a detection threshold. These observations suggest that during the minimum moonquake activity periods, the ultimate

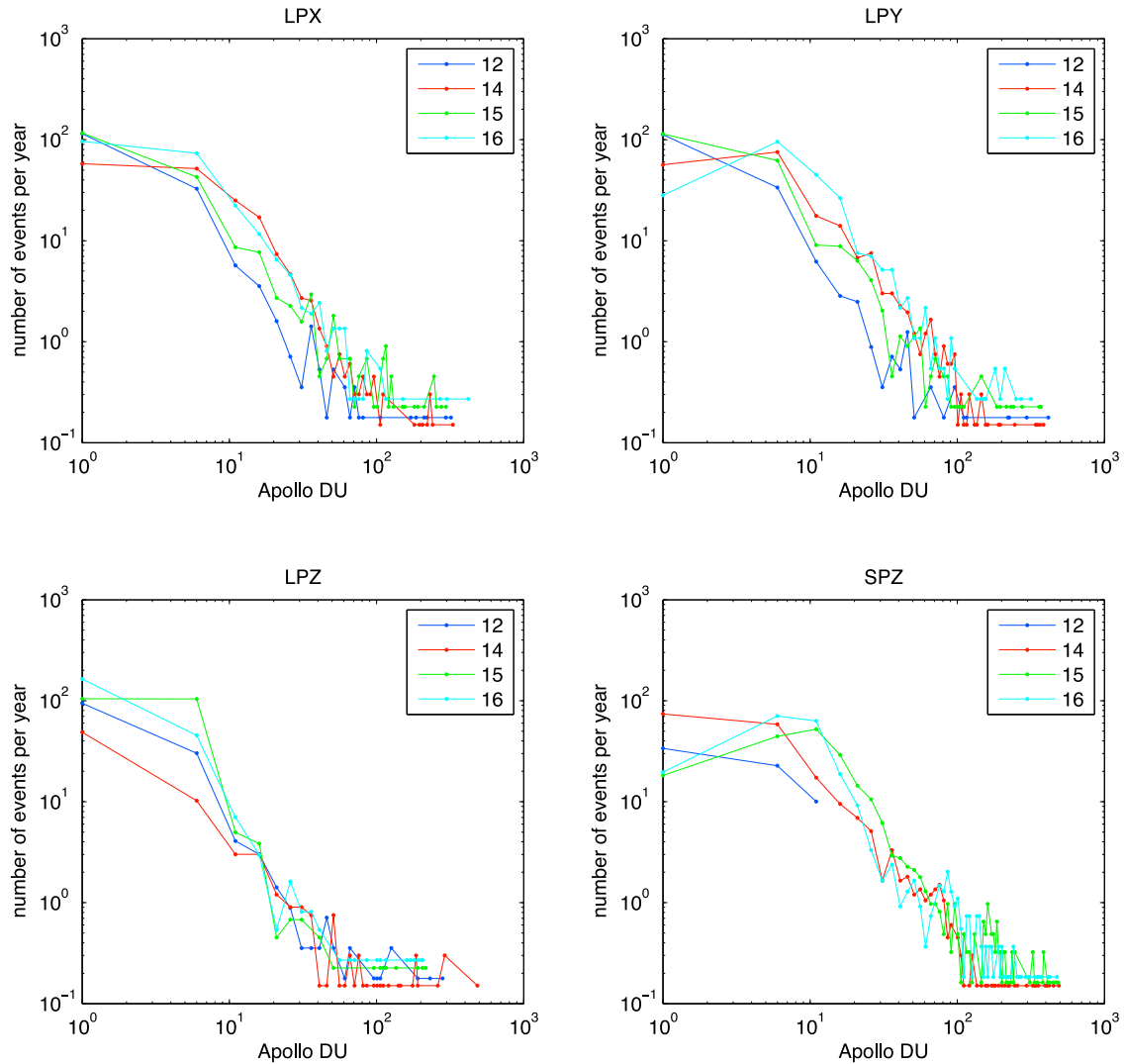


**Figure 2.** Number of impacts per year in peaked response mode with a given peak-to-peak amplitude (in Apollo DU) on the LP channels of all four stations. The SP statistics are shown for comparison; note that the SP component of station 12 failed early into the experiment.

background seismic noise of the Moon will very likely be related to the seismic signals of impacts.

### 3. Generation and Calibration of Impact Waveforms

[12] To estimate the seismic background noise due to impacts, we compute synthetic seismograms that depend on the parameters describing each impactor (the mass  $m$ , velocity vector  $\mathbf{v}$ , and impactor density). We calibrate the synthetics using the relevant characteristics of the artificial impacts recorded during the Apollo program, accounting for the density difference between rocky impactors and the almost empty spacecraft/rockets. This calibration process involves the following steps:

[13] 1. We calculate the seismic amplification that results from the production of ejecta (section 3.1). We simulate the cumulative distribution functions for the mass and momentum of the ejecta as a function of ejecta velocity for impactors with different velocities, densities and impact angles. The approach assumes that the source time durations are less than

the periods of typically observed body waves, and we justify this assumption quantitatively. We also justify our neglect of the seismic radiation pattern in our calculations.

[14] 2. We account for wave propagation effects due to intrinsic attenuation and diffraction (scattering), by modeling the waveform envelopes for the artificial impacts (section 3.2).

[15] 3. These considerations allow us to generate synthetic seismograms for an impactor of a given velocity and mass, at any epicentral distance  $\Delta$  (section 3.3).

#### 3.1. Modeling the Seismic Source

[16] The first consideration necessary to calibrate our synthetics is the source excitation process related to impacts. Several papers have addressed the efficiency of meteorite impacts in generating seismic waves on the Moon [Laster and Press, 1968; McGarr et al., 1969; Latham et al., 1970a], while others have addressed this problem on asteroids [Walker and Huebner, 2004; Ball et al., 2004; Richardson et al., 2005] and on Jupiter [Ingersoll et al., 1994; Lognonné et al., 1994]. In attempts to predict the number of impacts

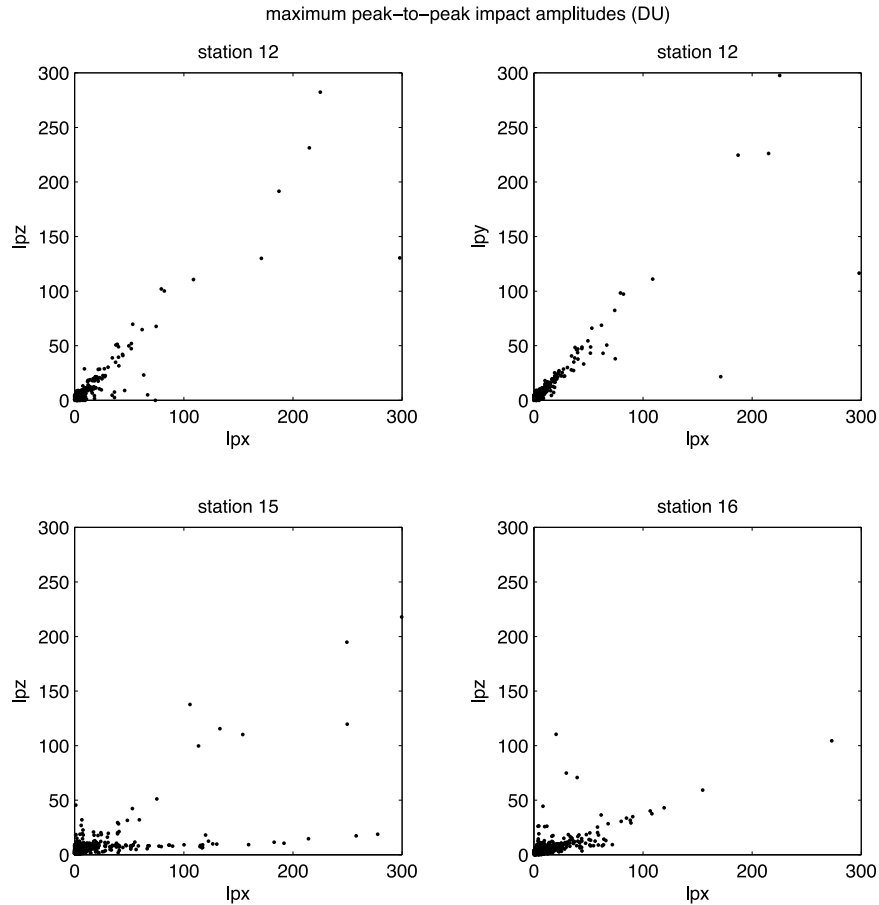


**Figure 3.** Comparison of LP vertical and horizontal (X component) peaked response mode impact amplitudes at Apollo stations 12, 15, and 16. In addition, the Y component amplitudes are shown for station 12.

potentially detectable by the Apollo ALSEP seismometers, *Laster and Press* [1968] used scaling equivalences between impacts and explosions, while *McGarr et al.* [1969] used an approach based on seismic force and seismic impulse. The latter is the approach we will use in what follows. We define the seismic impulse  $\mathbf{I}$  as the time-integrated force acting on the lunar surface during the impact:

$$\mathbf{I} = \int_0^{\tau} \mathbf{f}(t) dt \quad (1)$$

where  $\mathbf{f}$  is the equivalent seismic force (hereafter referred to as the seismic force) [see *Aki and Richards*, 2002] and  $\tau$  is the source duration time. This impulse is by definition equal to the momentum transferred to the source area. We define the momentum or seismic amplification  $S$  as

$$S = \frac{I}{mv} \quad (2)$$

where  $I = |\mathbf{I}|$  is the magnitude of the seismic impulse,  $m$  is the impactor mass,  $\mathbf{v}$  is the impactor velocity and  $v = |\mathbf{v}|$  is the magnitude of the impactor velocity. As noted by *McGarr et al.* [1969], for a perfectly inelastic impact where all the

velocity of the impactor is lost,  $\mathbf{I} = m\mathbf{v}$  and the seismic amplification value is 1. For a perfectly elastic impact where the impactor rebounds normal to the surface,  $\mathbf{I} = 2m\mathbf{v}$  and this value is 2. For hypervelocity impacts, where part of the energy release is related to the damage of both the impactor and the impacted surface, the seismic amplification can be between 1 and 2, or even larger than 2 due to ejecta. *McGarr et al.* [1969] reports values between 1 and 2 for impacts in sand, and values from 5 to 33 in bonded sands, with large experimental dispersion. In a different problem (related to asteroid mitigation) *Holsapple* [2004] finds momentum amplification factors of 1.11 and 10.6 for rocks impacting on porous or nonporous material respectively, when assuming that the ejecta travel at an angle of  $45^\circ$  with respect to the vertical of the impacted surface. *Holsapple* [2004] assumes moreover that such properties are valid for velocities in the range of 10 km/s to 40 km/s.

[17] In numerical impact experiments simulating 0.1 kg copper impactors on aluminium targets, *Walker and Huebner* [2004] obtained the following power law relation for the total momentum  $I_z$  perpendicular to the impacted surface:

$$\frac{I_z}{mv} = 0.97 \left[ \frac{v}{v_0} \right]^{0.27} \quad (3)$$

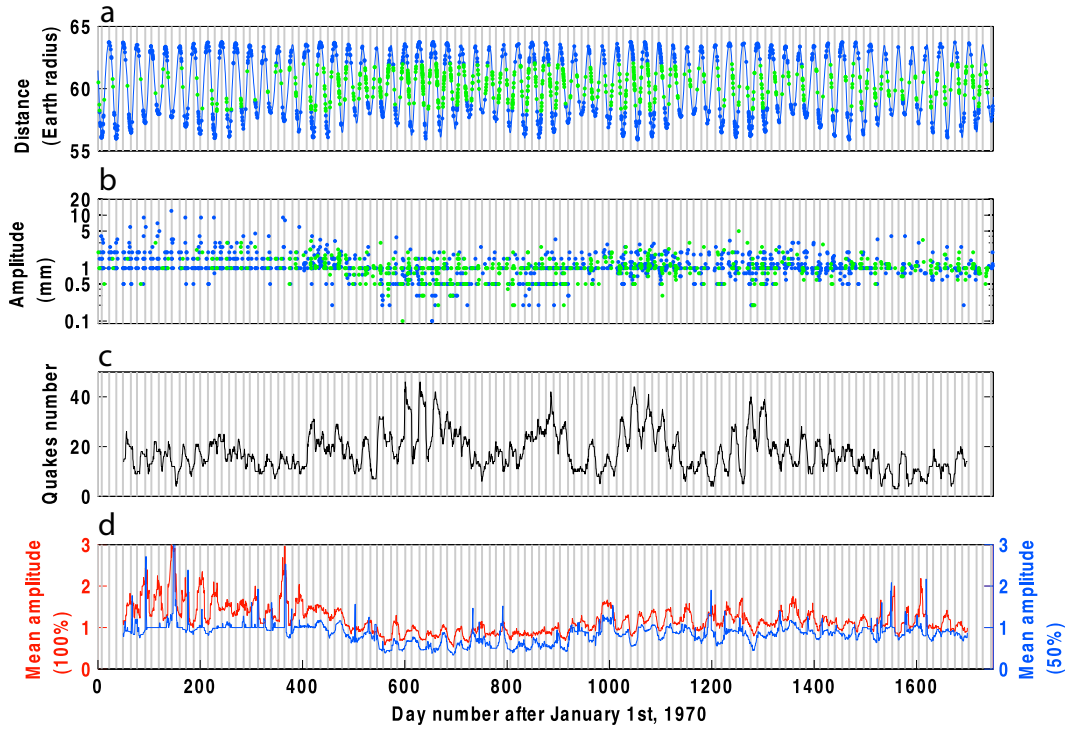


**Figure 4.** (a) Occurrence times of deep moonquakes plotted on the Earth-Moon distance curve. The green (blue) stars are used for events occurring when the Earth-Moon distance is smaller (greater) than 50% of its maximum excursion from the mean distance. (b) The corresponding amplitudes. (c) The number of moonquakes occurring in a 2 week period centered on any given day. (d) The mean amplitude of all events (red line) in this 2 week period, and the mean amplitude of the smallest 50% of events in the same period (blue line). We note variations in the latter between 0.5 to 1 mm.

where  $v_0$  is a constant taken to be equal to 1 km/s [see *Walker and Huebner*, 2004, equation (11.6)]. The ratio in equation (3) is the seismic amplification coefficient,  $S$ , under the assumption that the impulse is perpendicular to the impacted surface. *Walker and Huebner* [2004] found values for  $S$  from 1.05 to 1.9, for impactor velocities between 1 km/s and 10 km/s. These velocities are comparable to the typical impact velocity of the LM (1.7 km/s) and of the SIVB (2.6 km/s). If equation (3) is used, this leads to seismic amplifications for the SIVB and LM of 1.12 and 1.25 respectively.

[18] We now use these results to compute the seismic efficiency  $\varepsilon$  of the impact, in terms of energy. This is defined as the ratio between the seismic energy radiated and the kinetic energy of the impactor. By using equation (9) of *McGarr et al.* [1969], the seismic energy  $E_s$  radiated by an impact can be written as

$$E_s = \frac{4 \pi^2 0.384 I^2}{\rho v_p^3 \tau^3} \quad (4)$$

where  $\rho$  and  $v_p$  are the density and P wave velocity of the target, respectively, and  $\tau$  is the source time duration (Note that equation (10) of *McGarr et al.* [1969] contains an error: the factor 0.384 in the denominator should read  $\sqrt{0.384}$ ). This gives a seismic efficiency  $\varepsilon$  of

$$\varepsilon = \frac{E_s}{E_i} = 8 \pi^2 0.384 S^2 \frac{m}{\rho v_p^3 \tau^3} \quad (5)$$

where  $E_i = \frac{1}{2} m v^2$  is the impactor kinetic energy and we have made use of equation (2) relating  $I$  and  $S$ . In the framework of their tests, *McGarr et al.* [1969] found a mean value for  $\varepsilon$  of  $7.6 \times 10^{-5}$  for bonded sand and about 1 order of magnitude smaller for sand, assuming values for the source time durations of a few milliseconds associated with projectile masses in the range of milligrams. Other reports provide values ranging from  $10^{-5}$  to  $5 \times 10^{-5}$  [*Latham et al.*, 1970a], while *Richardson et al.* [2005] use two extreme values ( $10^{-6}$  and  $10^{-4}$ ).

[19] While the results of the above experiments take the contribution of the ejecta into account, the target properties and impactor sizes are not fully representative of the lunar surface, lunar gravity, and size of meteorites detected by the Apollo seismometers. Rather than simply extrapolate these results, we model the seismic force for natural impacts on the Moon as described below.

[20] Typical meteorite impacts on the Moon range in mass from a fraction of a kilogram to several tons. For all these impacts, the seismic source area (where nonelastic shock waves and fracturing occur) is confined to the first hundred meters below the surface, where P wave velocities of about 300 m/s can be assumed [*Lognonné and Mosser*, 1993]. For very small impacts (masses  $< 1$  kg), the value of the P wave velocity of the first few meters of the regolith is probably adequate (100 m/s). These speeds are close to those of the sand tests of *McGarr et al.* [1969], and suggests a seismic efficiency on the order of  $10^{-5}$ . The source duration time, which is associated with shock wave propagation, is typically

much shorter than a second. For an impact into the lunar regolith, assuming a P wave velocity of 300 m/s, a target density of 2000 kg/m<sup>3</sup>, a seismic efficiency of  $\varepsilon = 10^{-5}$  and an amplification  $S = 2$ , equation (5) gives a source time duration of 0.35 sec for an impactor of diameter 0.5 m and density 3000 kg/m<sup>3</sup>. A source time duration of 1 sec is achieved only for the large and rare impactors with diameters larger than 1.5 m (and weighing 5 tons or more). Thus the primary seismic source associated with the shock wave due to the impact, and the ejection of ejecta, are completed in a time much smaller than the typical periods of the waves recorded by the long-period instrument (these periods were greater than 1 sec, and the central frequency of the Apollo LP seismometer was 2 s). If the seismic efficiency is larger, most of the energy is radiated at high frequencies (above 1 Hz) and this implies a smaller source time. In contrast, for the short-period seismometers (1–50 Hz) the cutoff effects of the finite source duration may have to be taken into account, leading to a much more complex problem. In this paper we consider only the long-period records of impacts, as described in section 2.

[21] Under this approximation, the long-period seismic force is obtained from the balance of kinetic momentum in the source area:

$$\mathbf{f}(t) = \mathbf{I} \delta(t) = [\mathbf{m}\mathbf{v} - \mathbf{p}_{ejecta}] \delta(t) \quad (6)$$

where  $\delta(t)$  is a delta function in time and has units of  $sec^{-1}$ . Note that the momentum transferred to the seismic source has the opposite sign of the momentum carried by the ejecta ( $\mathbf{p}_{ejecta}$ ).

[22] In order to compute the momentum of ejecta, we use the scaling law proposed by *Holsapple* [1993]. From this paper, let us recall that the general properties of impact processes show that two regimes, called the strength and gravity regimes, may occur (see *Holsapple* [1993] for definition of these regimes). Equation (19) of *Holsapple* [1993] gives us the way to compute the transition value, in term of impactor radius, between these two regimes. We take the high velocities of the meteorites (i.e., 20 km/s), a regolith density of 1900 kg m<sup>-3</sup>, a cohesion and friction angle of 500 kPa and 45 degrees (see pages 499 and 506 of *Carrier et al.* [1991]) and a lunar gravity of 1.63 m s<sup>-2</sup>. This leads to a transition radius of about 1 mm, for the smallest impacts affecting the first 10 cm, to about 3 mm affecting the first half meter of regolith. As we will see later, the minimum mass of the considered impactors will be 1 gram (about 5mm in radius) and the latter generates a crater with a typical depth of 10 cm. We will therefore consider that the crater's properties generated by our impactors will all be in gravity regimes and can be represented by a single scaling law.

[23] By using equation (19) and *Holsapple* [1993, Table 2] or *Housen et al.* [1983, Table 1], we can show that the relative mass (in impactor mass units) of the ejecta with a velocity larger than a given value  $u$  can be expressed as a power law:

$$M_{>u}(u) = k \times \left(\frac{u}{v}\right)^{-\gamma} \quad (7)$$

where  $v$  is the impactor velocity and  $k$  and  $\gamma$  are constants depending on the impacted and impactor materials, as well as

the gravity and atmospheric properties of the impacted material. This relation has been used extensively in several papers; *Holsapple and Housen* [2007, Table 1 and Figure 1] provide example values for  $k$  and  $\gamma$  for several impact conditions, as well as the report from experiments.

[24] For rocky impacts on porous material (asteroids), *Holsapple* [2004] found values for  $k$  and  $\gamma$  of 0.005 and 1.4 respectively, and for nonporous material, 0.06 and 1.65 respectively. We use the impact model of *Holsapple* [1993] and the associated HTML software, available at <http://keith.aa.washington.edu/craterdata/scaling/index.htm>, to estimate the ejecta mass velocity relationship for rocky impacts on the lunar regolith. Figure 5a shows the cumulative ejecta mass for a rocky impactor (diameter 0.5 m and density 3000 kg/m<sup>3</sup>) incident at a 45° angle. Results are computed for three impact velocities (2.5 km/s, 10 km/s, and 20 km/s) and we find a good least squares fit with  $\gamma = 1.22$  and  $k = 0.047$ . Hence, ejecta with a velocity larger than the impact velocity have a total mass equal to 4.7% of the impactor mass, while more than 13 times the impactor mass is ejected with velocities larger than 1% of the velocity of the impactor. We find that  $k$  depends strongly on the incidence angle, varying from  $k = 0.0083$  to  $k = 0.0720$  for impact angles between 80° and 10° with respect to vertical. In contrast,  $\gamma$  is insensitive to incidence angle (varying from 1.22 to 1.23). These values are close to those reported in the work of *Holsapple and Housen* [2007, Table 1]. As equation (7) cannot be extrapolated to zero velocities, we compute the magnitude of the cumulative ejecta momentum,  $p_{<u}(u)$ , having velocities less than  $u$ , as follows (by numerical integration):

$$p_{<u}(u) = - \int_{u_0}^u \frac{dM_{>u}(u')}{du} u' du' = k \gamma v^\gamma \int_{u_0}^u (u')^{-\gamma} du' \quad (8)$$

where  $u_0$  is small enough in order to have  $M_{>u}(u_0) = M_{Total}$ , where  $M_{Total}$  is the full mass of the ejecta. This cumulative momentum is shown in Figure 5b. We find that the ejecta transport a total momentum which can be expressed as the following power law:

$$\frac{p_{ejecta}}{mv} = \eta \left[\frac{v}{v_0}\right]^{0.22} \quad (9)$$

As before  $m$  and  $v$  are the impactor mass and velocity and  $v_0$  is a constant set to 1 km/s. The parameter  $\eta$  is the ejecta contribution coefficient, which has a value for rocky impacts of about 0.63 (Table 1), but varies with impactor density and impact angle (Table 1). The artificial impacts can be modeled by low-density impactors (Table 1), as the spacecraft at the time of impact had almost empty tanks.

[25] The SIVB impacts generate about 1.67 times less ejecta than an impact of rocks with the same mass. For the LM impacts, we find very little ejecta (only about 2.5% of the impactor mass). This leads to different  $\eta$  coefficients: for the SIVB and LM impacts, we calculate values of 0.39 and 0.02 (Table 1). Differences are also found between rocky impactors and cometary impactors: a 20 km/s rocky impactor of 0.5 m in diameter generates  $5.27 \times 10^5$  kg of ejecta, while an icy one with the same mass and velocity generates  $4.28 \times 10^5$  kg, about 1.23 times less. The ratio of the ejecta momentum with respect to the impactor momentum,

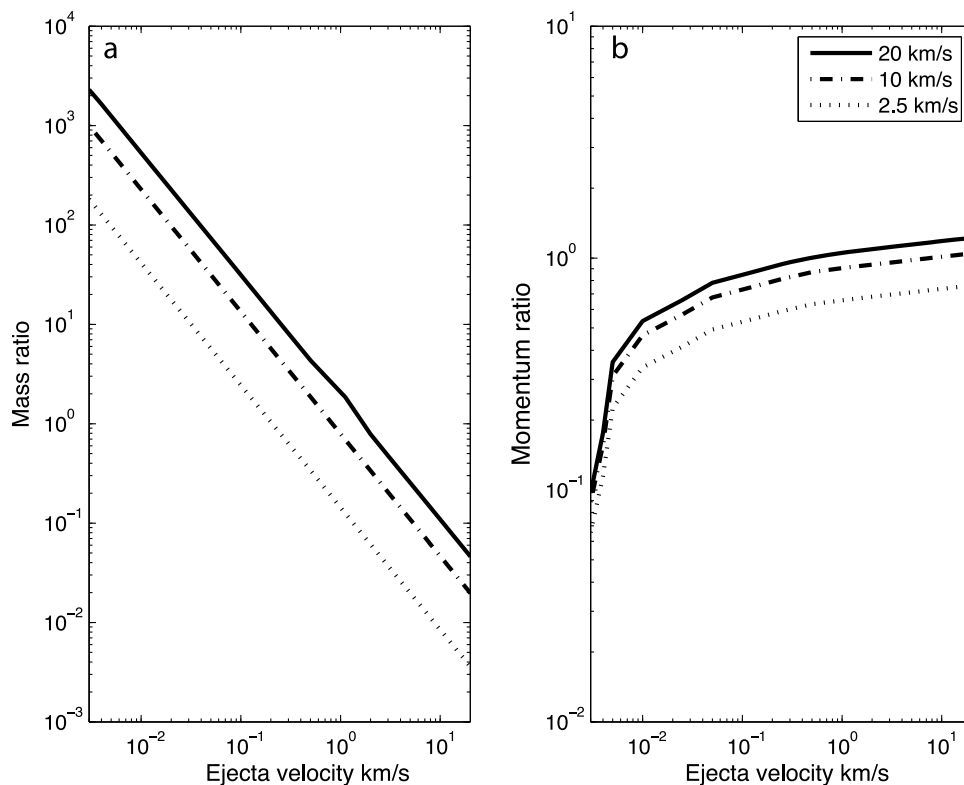


**Figure 5.** (a) Cumulative ejecta to impactor mass ratio and (b) momentum ratio. The different curves are for mean impactor velocities of 2.5 km/s, 10 km/s, and 20 km/s. Ejecta are computed with the model of *Holsapple* [1993] for an impact angle of  $45^\circ$ . The density and diameter of the impactor were set to  $3000 \text{ kg/m}^3$  and 0.5 m, respectively. Note that Figure 5a gives the relative mass of ejecta having their velocity greater than a given value  $u$  (equation (7)), while Figure 5b gives the momentum for all ejecta smaller than a given value  $u$  (equation (8)).

however, are very similar for a rocky impactor at 20 km/s and an icy one at 30 km/s: 1.24 versus 1.22 respectively (Table 1).

[26] The seismic amplification factor must also take into account the ejection angle of the ejecta with respect to the surface. *Edwards et al.* [2008] and *Yamamoto* [2002] found

experimental values ranging between  $30^\circ$  and  $38^\circ$  while *Holsapple* [2004] assumes a value of  $45^\circ$ . We choose a value of  $35^\circ$  and assume that the ejecta have an isotropic azimuthal distribution. Using the approach below, the lower and upper limits of  $30^\circ$  and  $45^\circ$  change our seismic amplification factor by  $-5\%$  and  $+10\%$  respectively. The total momentum of the

**Table 1.** Impactor Characteristics for Different Types of Impactors<sup>a</sup>

Type	Impactor Characteristics					Crater Characteristics				Source Characteristics		
	Angle ( $^\circ$ )	Velocity (km/s)	Mass (kg)	Density ( $\text{kg/m}^3$ )	Diameter (m)	Crater Diameter (m)	Rim Diameter (m)	Depth (m)	Formation Time (sec)	Ejecta Mass (kg)	Ratio	$\eta$
LM	86.3	1.68	2380	43.8	4.7	5.0	6.5	1.37	0.94	$1.43\text{E} + 04$	0.0245	0.02
SIVB	21	2.54	14000	23.7	10.4	22.9	29.8	6.25	2	$1.36\text{E} + 06$	0.483	0.39
Rocks	45	2.54	14000	3000	2.1	27.2	35.3	7.41	2.18	$2.27\text{E} + 06$	0.864	0.70
Ices	45	2.54	14000	800	3.2	25.3	32.9	6.91	2.10	$1.83\text{E} + 06$	0.677	0.55
Rocks	45	2.5	196	3000	0.5	8.1	10.5	2.2	1.18	$5.88\text{E} + 04$	0.772	0.63
Rocks	45	10	196	3000	0.5	13.1	17.1	3.6	1.51	$2.55\text{E} + 05$	1.05	0.63
Rocks	45	20	196	3000	0.5	16.7	21.7	4.6	1.71	$5.27\text{E} + 05$	1.24	0.64
Ices	45	30	196	800	0.77	17.93	23.3	4.9	1.77	$6.52\text{E} + 05$	1.22	0.58

<sup>a</sup>The two first lines are for the Apollo 12 LM and Apollo 14 SIVB impacts. The impactor shapes were modeled as spheres having volumes equal to that of cylinders, with diameters of 6.58 m and 4.3 m, and heights of 17.37 m and 3.76 m for the SIVB and LM impacts, respectively. SIVB sizes are from Y. Nakamura (personal communication, 2009). LM sizes are from NASA Apollo Module (LM) News reference, a report from Grumman Aircraft Engineering Corporation, page 19, [1968], see <http://history.nasa.gov/alsj/alsj-LMdocs.html>. The next six lines are for natural impactors. The first two represent impactors with masses equal to that of the SIVB but with densities of rocks and comets, while the last four represent smaller rocky impactors with different velocities and a comet (icy) impactor with an impact velocity of 30 km/s. Impact parameters are the angles with respect to vertical, velocity, mass, density, and diameter. The resulting crater characteristics are the crater diameter, the rim diameter, the depth of the crater and the formation time. The last three columns show the ejecta mass, ratio of ejecta momentum to the impactor momentum, and the parameter  $\eta$  from equation (9) when a dependence of  $v^{0.22}$  is assumed. All ejecta and source characteristics were computed with the software of *Holsapple* [1993], while the momentum ratio is computed through numerical integration of these results.

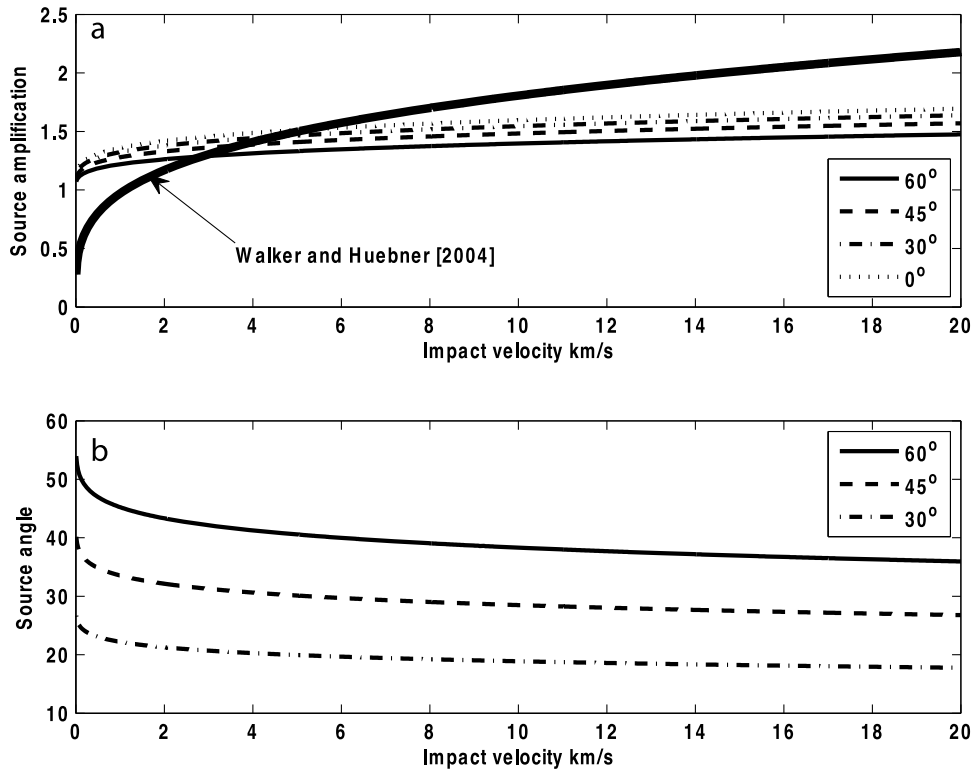


**Figure 6.** Seismic source parameters versus impact velocity. (a) The source amplification (equation (12)) for different impactor incidence angles (measured with respect to the surface normal). The model of *Walker and Huebner* [2004], valid for normal incidence ( $0^\circ$ ), is given for comparison. (b) The incidence angle of the seismic force or impulse for different impactor incidence angles as a function of velocity.

ejecta is therefore normal to the impacted surface and can be written in vector form as

$$\mathbf{P}_{\text{ejecta}} = -\sin(35^\circ) \times P_{\text{ejecta}} \mathbf{e}_z \quad (10)$$

where  $\mathbf{e}_z$  is the ingoing normal vector to the surface. By using equations (6), (9), and (10), and  $\sin(35^\circ) = 0.57$ , we can express the seismic impulse in vector form:

$$\frac{\mathbf{I}}{mv} = \mathbf{e}_v + \eta \times 0.57 \left[ \frac{v}{v_0} \right]^{0.22} \mathbf{e}_z \quad (11)$$

where  $\mathbf{e}_v = \frac{\mathbf{v}}{v}$  is the unit vector of the impactor velocity. By taking the norm of equation (11) and making use of equation (2), we finally get the nondimensional seismic amplification  $S$  as a function of  $v$  and  $\psi_v$ , the impact angle of the impactor with the normal to the impacted surface:

$$S(v, \psi_v) = \sqrt{1 + 2\eta \times 0.57 \left[ \frac{v}{v_0} \right]^{0.22} \cos \psi_v + \left( \eta \times 0.57 \left[ \frac{v}{v_0} \right]^{0.22} \right)^2} \quad (12)$$

where  $\mathbf{e}_v \cdot \mathbf{e}_z = \cos \psi_v$ . We also obtain the seismic force incidence angle, given by

$$\cos \psi_I = \frac{\cos \psi_v + \eta \times 0.57 \left[ \frac{v}{v_0} \right]^{0.22}}{S(v, \psi_v)} \quad (13)$$

The ejecta always amplify the vertical component amplitude, but only slightly for the LM impact due to the small value of  $\eta$ . Figure 6a shows these effects for rocky impactor velocities ranging from 1 to 20 km/s. We get an amplification between about 1.5 and 1.7 for impacting velocities of 20 km/s and impact angles between  $0^\circ$  and  $60^\circ$ .

[27] The amplification is larger for the model of *Walker and Huebner* [2004]. When extrapolated to the high 60 km/s impact velocities associated with retrograde impactors, we get an amplification factor of about 1.88 for an impact normal to the surface. In the case of oblique impacts, the major effect is a change in the direction of the associated seismic impulse; the direction of  $\mathbf{I}$  is closer to the surface normal than is the impactor velocity direction  $\mathbf{v}$  (Figure 6b). For a 20 km/s impact at  $45^\circ$  with respect to vertical, the angle of the impulse is about  $27^\circ$ , while for an impact angle of  $30^\circ$ , it is  $18^\circ$ . These impulse angles are in the two cases comparable to the SIVB impulse angle, very close to the impact angle due to the SIVB low impact velocity. For a horizontal impact, the extrapolation of equation (13) gives an impulse angle of  $55^\circ$ .

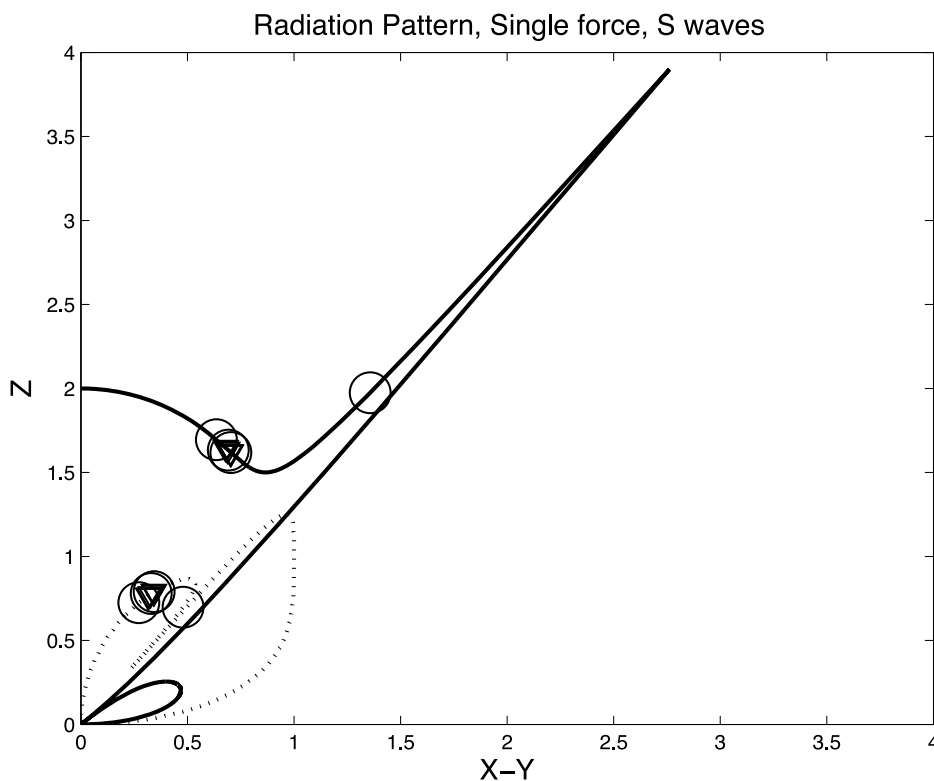


**Figure 7.** Nondimensional radiation pattern for the S waves generated by a seismic force, following Gupta [1966]. Shown are the relative amplitude variations as a function of the emitted ray direction. The emitted ray directions are the vectors (not represented) joining the origin and the circles and triangles for the LM and SIVB impacts, respectively. These angles have been computed using the lunar seismic velocity model of Gagnepain-Beyneix *et al.* [2006] and the impacts and station locations of Lognonné *et al.* [2003]. X and Y are the horizontal directions and Z is depth, both plotted using the same arbitrary units. The solid line is for a horizontal seismic force, while the dotted line is for a vertical seismic force.

[28] In addition to the impact direction, the other source parameter affecting the source emission is the radiation pattern of the seismic force or impulse, which depends not only on the impulse angle, but also on the angle of the departure ray and hence on the epicentral distance. The latter is given by Gupta [1966] for both P and S waves. These radiation patterns depend on the incidence angle of the P and S rays, which, for a given seismic model of the Moon, can be estimated from the epicentral distance between source and receiver. Figure 7 shows the theoretical radiation patterns for the S wave, for both a vertical and horizontal impulse, with the artificial impacts plotted according to epicentral distance. We observe that the seismic ray departure angle (and hence the incidence angle) is not strongly dependent on the epicentral distance: values range from about 20 to 35 for the model of Gagnepain-Beyneix *et al.* [2006], used here, with the epicentral distances ranging from about 70 km to 1750 km. We therefore do not model the effects of the radiation pattern, and assume the P and S wave incidence angles are the same for all impacts.

### 3.2. Propagation Effects

[29] The second consideration in calibrating our synthetics is the effect of scattering on seismic wave propagation. It has been shown that scattering is one of the most important features observed in the lunar seismograms [Latham *et al.*, 1970b, 1971] and that the maximum amplitude of the

waveform is reached in the coda of the S waves. An exact description of the scattering process from the elastic wave equation is difficult, thus only approximations have been used, such as diffusion theory [Dainty *et al.*, 1974; Dainty and Toksoz, 1977; Nakamura, 1976, 1977] or seismic quanta scattering theory [Strobach, 1970], where the signal is interpreted as the summation of all possible raypaths in a heterogeneous body. These two theories give equivalent expressions for the seismic signal. We use the formulation of Strobach [1970] to model the variation in the amplitudes of impact-generated waves with epicentral distance. In this approach, the envelope of the signal's energy is proportional to

$$e(t) = A^2 q^{\alpha t} \frac{1}{\alpha t} e^{-\frac{1}{\alpha t} \frac{\Delta^2}{\sigma^2}} \quad (14)$$

where  $A$  is an amplitude parameter (and hence  $A^2$  is an energy parameter) that depends on the source and instrument,  $q$  is a positive attenuation factor smaller than 1,  $\alpha$  is a propagation parameter,  $\Delta$  is the epicentral distance, and  $\sigma$  is the diffusion length scale (see Strobach [1970] for detailed descriptions of these parameters). We parameterize the attenuation factor such that  $q = 1 - 10^{-q_0}$ , with the intent of investigating a wide range of attenuation factors by searching over a range of values for  $q_0$ . The amplitude envelope  $a(t)$  of the signal is given by  $a(t) = \sqrt{e(t)}$ .

**Table 2.** Impact Parameters for the Artificial Impacts Recorded by the Apollo Seismometers<sup>a</sup>

Impact	Date	Latitude (°)	Longitude (°)	Velocity (km/s)	Angle (°)	Distance From Stations				Kinetic Energy (erg)	mv (kg.m/s)
						S12 (km)	S14 (km)	S15 (km)	S16 (km)		
12LM	20 Nov 1969	3.94S	21.20W	1.68	86.3	<b>73</b>	-	-	-	$3.36 \times 10^{16}$	$0.4 \times 10^7$
13SIVB	15 Apr 1970	2.75S	27.86W	2.58	14	<i>135</i>	-	-	-	$4.63 \times 10^{17}$	$3.59 \times 10^7$
14SIVB	04 Feb 1971	8.09S	26.02W	2.54	21	<i>172</i>	-	-	-	$4.52 \times 10^{17}$	$3.56 \times 10^7$
14LM	07 Feb 1971	3.42S	19.67W	1.68	86.4	<b>114</b>	67	-	-	$3.35 \times 10^{16}$	$0.39 \times 10^7$
15SIVB	29 Jul 1971	1.51S	11.81W	2.58	28	<b>355</b>	184	-	-	$4.61 \times 10^{17}$	$3.57 \times 10^7$
15LM	03 Aug 1971	26.36N	0.25E	1.70	86.8	1130	1048	<b>93</b>	-	$3.44 \times 10^{16}$	$0.41 \times 10^7$
16SIVB	19 Apr 1972	1.30N	23.80W	2.5–2.6	21	<b>132</b>	<i>243</i>	<b>1099</b>	-	$4.59 \times 10^{17}$	$3.6 \times 10^7$
17SIVB	10 Dec 1972	4.21S	12.31W	2.55	35	<b>338</b>	<i>157</i>	<b>1032</b>	850	$4.71 \times 10^{17}$	$3.69 \times 10^7$
17LM	15 Dec 1972	19.96N	30.50E	1.67	85.1	<b>1750</b>	<i>1598</i>	<b>770</b>	985	$3.15 \times 10^{16}$	$0.38 \times 10^7$

<sup>a</sup>Toksoz et al. [1974]. All data are related to tracking information except those of Apollo 16 SIVB, whose estimates are based on the interpretation of seismic data due to a premature loss of tracking information. The angle value provides the geometry of the impact with respect to the surface normal. The impacts used for the calibration of our synthetics are indicated in bold. Those in italics were not used, due to various instrument problems (the vertical data recorded at station 12 for the SIVB impacts of Apollo 13 and Apollo 14 were saturated, and the vertical component of station 14 was no longer in operation for the impacts of Apollo 16 and 17). Impacts listed in plain font were not used due to their small amplitudes, as their waveforms were too strongly affected by the digitization noise. All data were recorded in peaked response mode, except the impact of the Apollo 12 LM, which was recorded in flat response mode. The amplitude of that impact has therefore been corrected by a factor two, corresponding to the mean sensitivity ratio of the two modes in the bandwidth 0.3–0.7 Hz.

[30] The amplitude parameter,  $A$ , of equation (14) depends on the seismic impulse, (developed in the previous section and equal to  $mv S(v, \psi_v)$ ). Ideally, it would be possible to fit the observed amplitude of the envelope function, using equation (14) and the seismic impulse formulation of the previous section. The parameters  $q$ ,  $\alpha$ ,  $\sigma$  depend upon lunar structure and  $A$  is different for each impact. However, because of the limitations of the diffusion theory, we shall see below that our estimate of  $\sigma$  depends on epicentral distance, and both the attenuation and diffusion parameters appear to depend upon whether the LM or SIVB impacts are considered. A full inversion of all waveforms for the parameters in equation (14) is unwieldy and so we take a two-step process. First we use the full waveforms to estimate  $A$  and  $\sigma$  for each impact. We establish the variation of  $\sigma$  with epicentral distance from this step, and use our values of  $A$  to estimate the maximum amplitude of each waveform. We then use equation (14), equation (16), and the development of the seismic impulse in section 3.1 to set up a relationship between the maximum amplitude of each seismogram and the attenuation and diffusion parameters (equation (17)). We then estimate attenuation and diffusion parameters for two sets of impacts (the LM and SIVB) using only the maximum amplitudes, not the full envelope function.

[31] For all the waveforms considered (i.e., the LP vertical component seismograms of the impacts listed in Table 2), we have determined the best set of parameters  $A$ ,  $q$ ,  $\alpha$ , and  $\sigma$ . We did this as follows: (1) calculate time relative to the P wave arrival time, (2) calculate the amplitude of the envelope function; the envelope is computed using a Hilbert transform, (3) use a 5 min running window, and take the median value between the running mean and the running maximum value (this was determined empirically to produce more stable results), (4) determine  $q$ ,  $\alpha$ ,  $\sigma$  and  $A$  for each artificial impact, by exploring a range of values for each parameter and minimizing the RMS misfit of the predicted envelope (equation (14)) to that calculated from the data.

[32] Figure 8 shows a typical envelope fit, for the impact of the Apollo 15 SIVB, as recorded on the station 12 LP vertical component. We find that the values for diffusion length scale  $\sigma$  for the artificial impacts are described

reasonably well by a power law dependence on epicentral distance (Figure 9):

$$\sigma = \sigma_0 \left[ \frac{\Delta}{\Delta_0} \right]^\beta \quad (15)$$

where  $\Delta_0$  is set to 100 km, a distance comparable to the LM source receiver epicentral distance. Note that the choice of  $\Delta_0$  does not matter, since  $\sigma_0$  varies as  $\Delta_0^{-\beta}$ . The SIVB impacts fit yields values for  $\sigma_0$  and  $\beta$  of 3.4 km and 0.80, and the LM impacts fit yields 2.5 km and 0.79. A combined fit to both the LM and SIVB impacts yields values of 2.8 km and 0.85 respectively, with a root-mean-square error of 25%.

[33] The dependence of the diffusion length scale  $\sigma$  on epicentral distance, as well as the imperfect fit of the decay of the coda (Figure 8) indicate limitations of equation (14), such as the 2-D approximation inherent in the theory [Strobach, 1970]. However, although above we have fit the full envelope waveform, our goal is mainly limited to modeling the variation in maximum amplitude with epicentral distance. The energy envelope reaches its maximum value  $e_m$  when  $\frac{d}{dt}e(t) = 0$ , or at time

$$t_m = \left[ \frac{1}{\alpha} \right] \frac{2}{1 + \sqrt{1 - 4 \ln(q) \left[ \frac{\Delta}{\sigma} \right]^2}} \left[ \frac{\Delta}{\sigma} \right]^2 \quad (16)$$

The maximum amplitude of the signal envelope is obtained by substituting  $t_m$  from equation (16) into equation (14), and calculating  $\sqrt{e(t_m)}$ . This maximum amplitude does not depend on the parameter  $\alpha$ . We use, for each seismogram, our estimated values of  $q$ ,  $\sigma$ , and  $A$  to compute this maximum amplitude  $A_{\max}$  for each artificial impact at  $t_m$ . We then assume that for any impact,  $A_{\max}$  is proportional to the seismic impulse (equal to  $mv S(v, \psi_v)$ ) and so we can write

$$A_{\max}(m, v, \psi_v, \Delta, q, \sigma, A_0) = A_0 \frac{mv}{10^7 N_s} S(v, \psi_v) a_m(\Delta, q, \sigma) \quad (17)$$

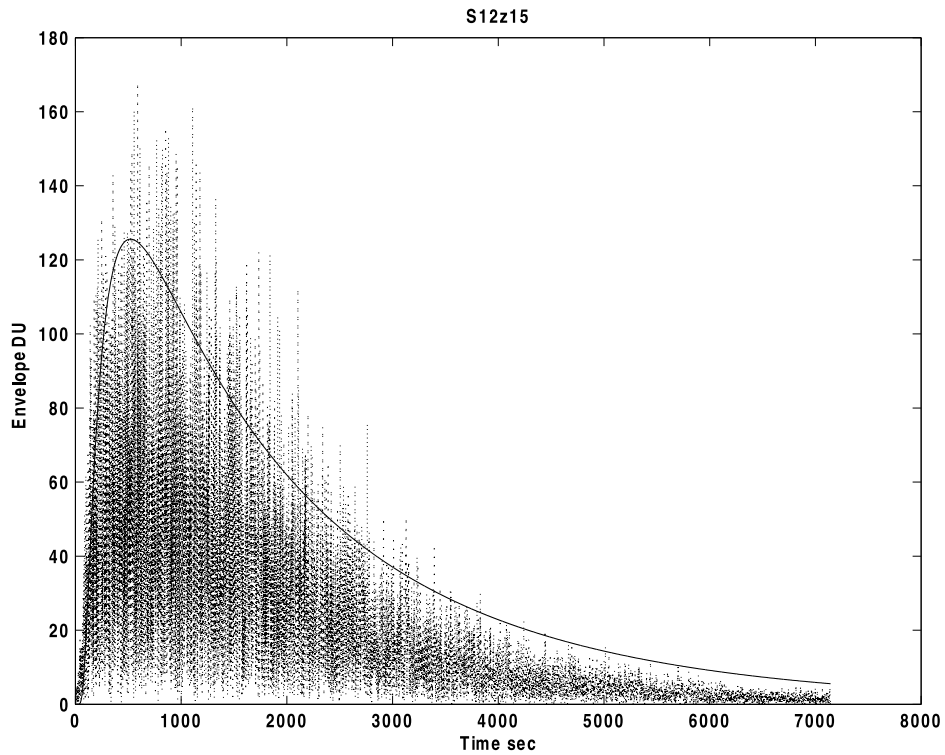


**Figure 8.** Typical waveform envelope fit, shown here for the impact of the Apollo 15 SIVB as recorded by the station 12 LP vertical component (epicentral distance of 355 km). In order to get more stable results, we fit the theoretical envelope using the median value between the running maximum of the envelope and its running mean value (in both cases defined for a window length of 300 s). The best fit was obtained by exploring the model space for all acceptable values of  $q$ ,  $\alpha$ ,  $\sigma$ , and  $A$ ; the residual misfit is typically a few percent.

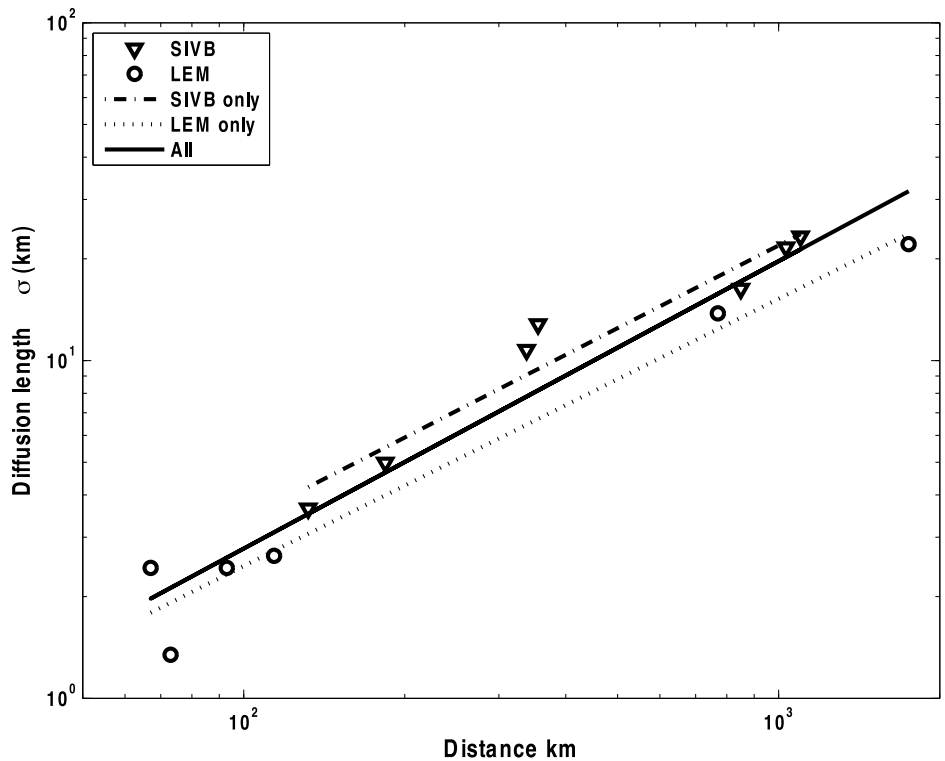


**Figure 9.** Distribution of the envelope diffusion length  $\sigma$  for all artificial impacts used. The diffusion length increases with the epicentral distance following a power law and likely reveals a systematic feature of lunar propagation.

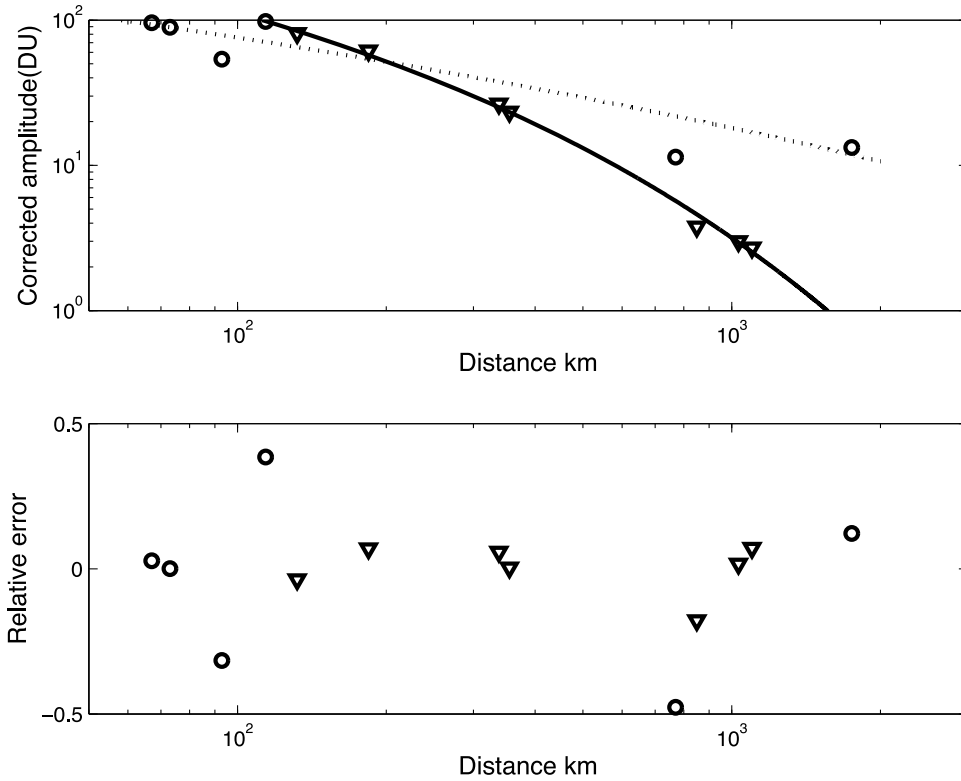


**Figure 10.** (top) Maximum envelope amplitudes for the LM impacts (circles) and the SIVB impacts (inverted triangles) as a function of epicentral distance. As the artificial sources had different impulses, the amplitudes are normalized with respect to an impact impulse of  $10^7$  Ns, by multiplying the amplitude by  $10^7/I$ , where  $I$  is given by equations (2) and (11) with  $\eta = 0.39$  for the SIVB impacts and 0.02 for the LM impacts. The dotted line displays the least squares solution for the theoretical fit using diffusion theory for the LM impacts (solid line, SIVB impacts). (bottom) The relative errors in both cases. The RMS errors are 28.6% for the LM impacts and 9% for the SIVB impacts.

where  $m$ ,  $v$ ,  $\psi_v$ , and  $S$  are the impactor mass, velocity, incidence angle and seismic amplification defined in equation (12),  $A_0$  is a constant, and  $a_m$  is now simply the functional form for the maximum value of the amplitude of the envelope function (obtained from equation (14) with  $A = 1$  and  $t = t_m$ ). In other words, the empirical scaling factor  $A$  of equation (14) has now been replaced by the functional form,  $A_0 \frac{mv}{10^7 Ns} S(v, \psi_v)$ , that describes the dependence of amplitude on the source excitation process, developed in section 3.1. As described above,  $a_m$  depends only on the epicentral distance  $\Delta$  and the parameters  $q$  and  $\sigma$  and  $\sigma$  has a power law dependence on  $\Delta$ . Note also that we have normalized the expression to a source of  $10^7$  Ns.

[34] Using the maximum amplitudes of the envelopes of the artificial impact waveforms determined in the first step ( $A_{\max}$ ) and the known impact velocity, angle and impactor mass, we calculate a least squares fit to equation (17) by exploring a range of values for  $A_0$ ,  $q$ ,  $\sigma_0$ , and  $\beta$ . We investigate the SIVB and LM impacts separately. The resulting fits between the envelope maximum and equation (14) are shown in Figure 10 and the parameter values are given in Table 3. These parameters fit the amplitudes fairly well (solid and dotted lines in Figure 10), with a mean square error of about 9% for the SIVB impacts, but a larger error of 28.6% for the LM impacts. A fit to both SIVB and LM amplitudes combined yields a larger a posteriori error of 82%. A large

misfit is obtained for the amplitude of the LM impact of Apollo 17, which is known to have impacted the South Massif [Kovach *et al.*, 1973] and may have released more seismic energy due to impacting harder rocks. If we exclude this impact, the a posteriori error for a single curve is still about 43% (i.e., larger than the errors found for the a posteriori fit with two different curves). In other tests, we used a simpler amplitude formulation, with only an inverse dependence on epicentral distance. The final results using the two methods were very comparable. Given these results, and the limited number of artificial impact waveform data, more detailed modeling of the dependence of amplitude on epicentral distance (e.g., 3-D diffusion theory) [Nakamura, 1977] is not currently warranted, and we do not think it would significantly change our final estimates of the microseismic noise generated by impacts.

[35] We propose that the differences between the LM and SIVB impacts are caused by the excitation processes. In the

**Table 3.** Results of the Fit for the Amplitude Dependence of the LM and SIVB Impacts

Impact	A (DU)	$\sigma_0$ (km)	$\beta$	$q_0$
SIVB	$1.13 \times 10^4$	3.43	0.53	2.56
LM	$3.07 \times 10^4$	2.22	0.84	2.43

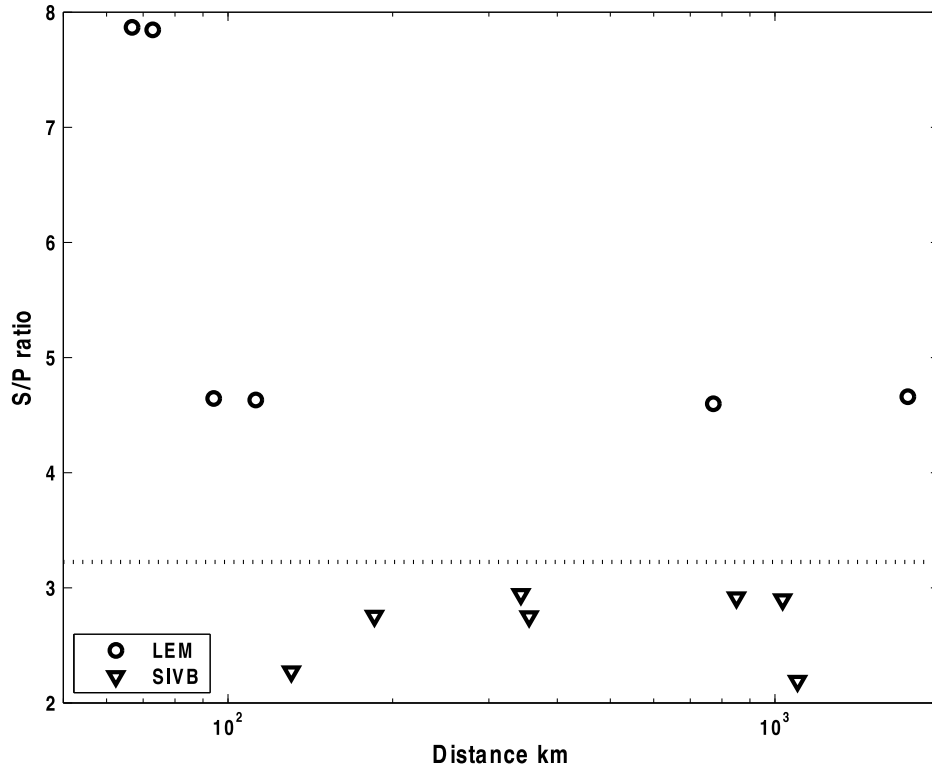


**Figure 11.** S to P amplitude ratio versus distance, as estimated from the radiation functions with subsurface P and S velocities of 1000 m/s and 500 m/s, respectively. Circles are for the LM impacts, while the inverted triangles are for the SIVB impacts. The dashed line is the S to P ratio in the diffusive regime for a mantle  $v_p$  to  $v_s$  ratio of  $\sqrt{3}$ .

full diffusion regime, the P and S wave energies are almost in equipartition, leading to the typical Apollo waveforms. In this case, *Papanicolaou et al.* [1996], following works of *Aki* [1992], have shown that the P to S seismic energy ratio is a constant value, given by

$$\frac{E_p}{E_s} = \frac{v_s^3}{2v_p^3} \quad (18)$$

where  $v_p$  and  $v_s$  are the P and S seismic velocities. For typical P and S velocities, this ratio is about 1/10 and the amplitude ratio is the square root of this value.

[36] Let us now compute the ratio of the amplitudes of S body waves to P body waves, estimated from the source parameters of the artificial impacts and compare it to  $\sqrt{\frac{2v_p^3}{v_s^3}}$ , in order to better understand the diffusion regime. We assume that the amplitudes of the S waves  $a_S$  are proportional to

$$a_S \sim \frac{m v S(v, \psi_v) (R_s^h(\theta, \psi_I) I_h + R_s^z(\theta, \psi_I) I_z)}{4\pi\rho v_s^2} \quad (19)$$

where  $\rho$  is the mean density of the impacted subsurface and  $R_s^h$  and  $R_s^z$  are the radiation functions of an impulse on the horizontal and vertical components respectively, given by *Gupta* [1966], which depend on the ray incidence angle  $\theta$  and the impulse direction  $\psi_I$ .  $I_h$  and  $I_z$  are the projections of the seismic impulse on the horizontal and vertical axes respectively. See Figure 7 for the S wave radiation functions.

A similar expression for the amplitude of the P body wave can be used, by using the P wave velocity ( $v_p$ ) and radiation function ( $R_p$ ), in place of  $v_s$  and  $R_s$  in equation (19). The result, in terms of the S wave to P wave amplitude ratio, is shown on Figure 11. We see that the LM impacts generate waves with an S/P ratio much larger than the diffusion regime ratio. Most of the coda is therefore created by the diffraction of the direct S wave. In contrast, the SIVB impacts excite body waves with an S to P ratio smaller than the diffusion regime, and the coda is therefore mainly created by the conversion of P waves to S waves. A preferential S excitation of LM impacts versus P excitations of SIVB impacts is also found in the amplitude data. The ratio between the terms  $A_0$  found for the LM and SIVB impacts ( $3.07 \times 10^4 / 1.13 \times 10^4 = 2.72$ ) is indeed close to the value of  $v_p^2/v_s^2$  in the regolith. We also have a ratio between the diffusion length found in these two cases ( $2.22 \text{ km} / 3.43 \text{ km} = 1/1.54$ ), which can be explained as a consequence of the smaller wavelength of the S waves as compared to the P waves (for which the ratio is about  $1/\sqrt{3}$ ). In both cases however, the attenuation is found to be quite similar (2.56 for SIVB, 2.43 for LM), since in both cases the S-generated coda is the most sensitive to attenuation processes.

[37] As most of the excitation terms are those of S waves for the LM, we cannot exclude that site amplification effects in the vicinity of the impacts might be responsible for the larger dispersion of the LM amplitudes. We note for example on Figure 10 (bottom) that the vertical long-period signal recorded at station 12 for the Apollo 14 LM impact (a distance of 114 km, see Table 2) is larger by a factor of almost

1.5 (a relative error of just under 50%) as compared to the theoretical curve given by equation (17). This impact was very close to the Apollo 14 site (67 km) and station 14 has a very large amplification on the horizontal component, as shown by the larger detection rate on Figure 2. Amplification of a horizontal source, such as the almost horizontal LM source, is therefore likely. The other deviation is observed for the Apollo 17 LM impact, and as noted above is probably related to the South Massif structure. These source effects are much weaker for P waves, which might explain the better agreement of the SIVB impacts with theoretical values.

### 3.3. Calculating Synthetics

[38] We now use these results to empirically model natural impacts. The natural impacts generally occur with much higher velocities than the artificial impacts, so that even for grazing impacts the ejecta generate a seismic force with an incidence angle smaller than 55 (see equation (12) for  $\psi_v = 0$ ), generally much closer to the SIVB impact geometry than the LM geometry. We therefore use the SIVB amplitude/distance curve as our reference, and assume that the impulse angle  $\psi_v = 0$ . As horizontal impacts may generate larger signals (the increase in amplitude due to the smaller value of shear velocity in equation (19) can be a larger effect than the decrease in seismic amplification factor in equation (12) due to the horizontal impact), our approach is therefore a lower bound on impact effects. In order to model the waveform of an impact occurring at a distance  $\Delta$ , we perform a linear combination of the two SIVB impact records with the closest epicentral distances ( $\Delta_1$  and  $\Delta_2$ ), by correcting the amplitudes using equation (17) for  $A_{\max}$ . The modeled signal is then

$$s(t - T) = A_{\max}(m, v, \psi_v = 0, \Delta) \cdot \left[ sn_1(t - T_1) + \frac{\Delta - \Delta_1}{\Delta_2 - \Delta_1} [sn_2(t - T_2) - sn_1(t - T_1)] \right] \quad (20)$$

where  $A_{\max}(m, v, \psi_v, \Delta)$  is computed using equation (17) for the chosen values of  $A_0$ ,  $q$ , and  $\sigma$  with a vertical seismic force such that  $\psi_v = 0$ .  $T$ ,  $T_1$  and  $T_2$  are the P wave travel times at epicentral distances  $\Delta$ ,  $\Delta_1$  and  $\Delta_2$  respectively, and  $sn_1(t) = \frac{s(t)}{A_{\max}(m_1, v_1, \phi_1, \Delta_1)}$  and similarly for  $sn_2$ , are the waveforms associated with the two closest SIVB impacts, normalized by  $A_{\max}$  for each impact. Note that implicit in equation (17) for  $A_{\max}$  is the different seismic amplification that results from density differences of the impactors: for the SIVB impacts we use  $\eta = 0.39$  while for the natural impacts, we use  $\eta = 0.63$  (Table 1). For impacts at distances larger than the maximum recorded SIVB distance (1099 km) or smaller than the minimum (132 km) (both associated with the Apollo 16 SIVB impact), we include only an amplitude correction and a P starting time shift for one artificial impact waveform. The corresponding waveform expression is therefore

$$s(t - T) = A_{\max}(m, v, \psi_v = 0, \Delta) sn_1(t - T_1) \quad (21)$$

where  $sn_1(t)$  is the closest artificial impact available. All P wave travel times at arbitrary distances were computed using the *Gagnepain-Beyneix et al.* [2006] lunar seismic model,

and the P wave travel times  $T_1$  and  $T_2$  for the artificial impacts are listed in the work of *Lognonné et al.* [2003].

## 4. Generating an Impact History

[39] We now need a model for the flux of impactors that includes impact time, location, mass, and velocity. We use the Near-Earth Objects (NEOs) model of *Bottke et al.* [2002], which provides a debiased estimate of the orbital distribution of bolides that can potentially encounter the Earth-Moon system. This model assumes that the NEO population is in steady state, being continuously replenished by the influx of material coming from source regions associated with the main asteroid belt or the transneptunian disk. The model was determined through extensive numerical integrations of test particles from these sources, and calibrated with the real population observed by the Spacewatch survey.

[40] Observations for objects with diameters ranging from  $\sim 10$  m to  $\sim 10$  km show no correlation between the size and orbital elements of the NEOs [*Stuart and Binzel, 2004*]. We assume that this lack of correlation also applies to the projectile masses considered in this study ( $\sim 1$  g to 1 ton, corresponding to diameters of  $\sim 1$  cm to 1 m). By doing so, we neglect the potential influence of the Yarkovsky effect, associated with the solar radiation pressure which might couple size with trajectory. Our assumption, that will be validated later in the text, allows us to study the statistical distribution of orbital parameters, including velocities, separately from the distribution of masses.

[41] We compute the orbital parameters  $a$ ,  $e$ , and  $i$  (the semimajor axis, eccentricity, and inclination, respectively) of each object using the method of *Opik* [1951]. For each  $(a, e, i)$  cell of the NEO model, we calculate the impact probability with the Earth and Moon, and the corresponding impact velocity. We assume that the apsides and nodes of all bodies precess uniformly, and we neglect Earth's orbital eccentricity (0.017, which amounts to a velocity variation of  $\pm 0.5$  km/s of the Moon and just under a 3% effect on the resulting seismic impulse). The Moon's orbit is considered Earth-like. For an object with a given  $(a, e, i)$  triad, the impact probability per year is

$$P(a, e, i) = \frac{R^2}{a_0^2} \left( 1 + \frac{v_{esc}^2}{v^2} \right) \frac{v}{|v_x|} \frac{1}{\pi \sin i} a^{-3/2} \quad (22)$$

with

$$\begin{cases} v_{esc}^2 &= 2GM/R \quad v_{orb}^2 = GM_S/a_0 \\ v^2 &= v_{orb}^2 \left( 3 - \frac{a_0}{a} - 2\sqrt{\frac{a}{a_0}(1-e^2)} \cos i \right) \\ v_x^2 &= v_{orb}^2 \left( 2 - \frac{a_0}{a} - \frac{a}{a_0}(1-e^2) \right) \\ v_y &= -v_{orb} \left( \sqrt{\frac{a}{a_0}(1-e^2)} \cos i - 1 \right) \\ v_z^2 &= v_{orb}^2 \frac{a}{a_0} (1-e^2) \sin^2 i \end{cases} \quad (23)$$

where  $G$  is the gravitational constant,  $M_S$  is the mass of the Sun,  $a_0$  is the semimajor axis of the Earth,  $M$  and  $R$  are the mass and radius of the target (i.e., the Moon or the Earth as both were done in order to calculate the Earth/Moon ratio),

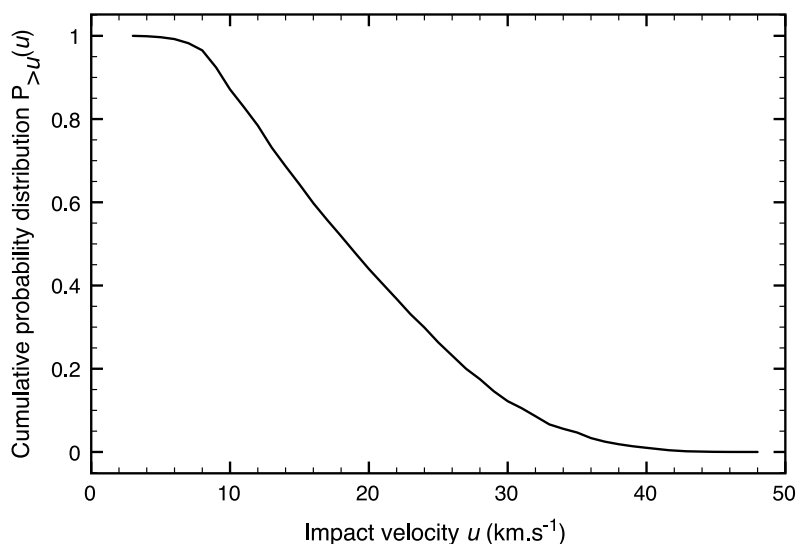


**Figure 12.** Complementary cumulative distribution function of impact velocity on the Moon. This gives the probability of an impact having a velocity larger than a given value.

$v_{esc}$  and  $v_{orb}$  are the escape and orbital velocity of the target, and  $v$  is the relative encounter velocity, referred as velocity at infinity, as it does not account for the gravitational influence of the target. The three components of  $v$  ( $v_x$ ,  $v_y$  and  $v_z$ ) are expressed in a frame ( $O_{xyz}$ ) centered on the target, where ( $O_{xy}$ ) defines the target's orbit plane, ( $O_x$ ) points toward the Sun and ( $O_z$ ) points upward. The associated lunar impact velocity, once the gravitational influence of the target accounted for, is  $u = \sqrt{v^2 + v_{esc}^2 + 2 \frac{GM_{earth}}{a_{moon}}}$ . Note that the last term under the square root corrects for the gravitational effects of the Earth on the lunar impact velocity, as the Moon has been treated as

an isolated body in space [Zahnle *et al.*, 2001]. Each cell produces an impact with a velocity probability proportional to  $P(a, e, i) \times n(a, e, i)$ , where  $n(a, e, i)$  is the relative number of objects in a cell (the absolute number depends on the mass considered). We obtain a cumulative distribution function of impact velocity that will be referred to as  $P_{>u}(u)$  (Figure 12) and shows the probability of an impact occurring with a velocity larger than  $u$ . The calculated average impact velocity on the Moon is 19.3 km/s, consistent with the value of 19.2 km/s reported by Stuart and Binzel [2004]. The relative impact rate on the Earth with respect to the Moon is found to be 1.6 times larger per unit area. The distribution  $P_{>u}(u)$

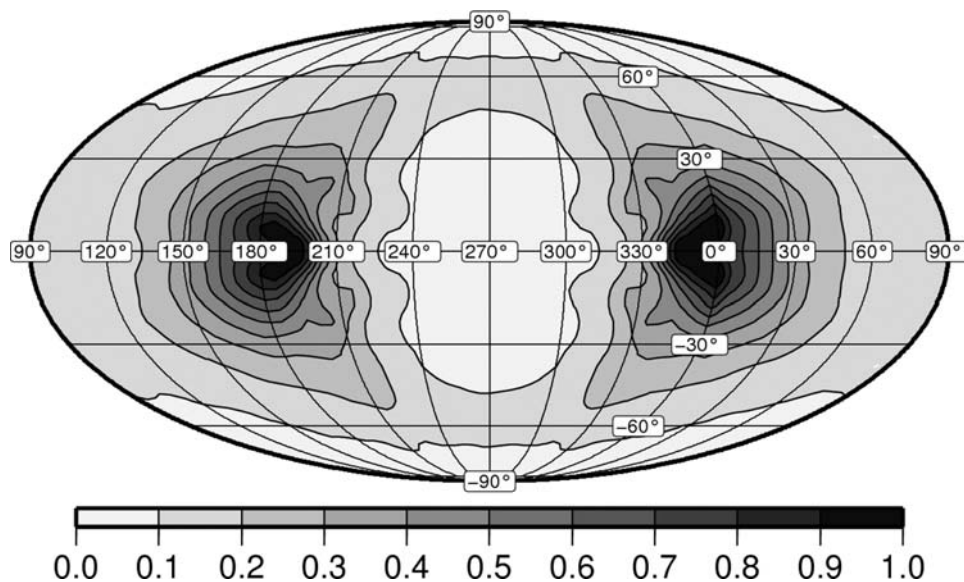


**Figure 13.** Probability distribution of the radiant direction of bolide encounters with Earth. Steady state estimate averaged over revolution and precession cycles. Latitude and longitude of arrival are expressed in a geocentric coordinate system, where ( $O_{xy}$ ) defines the Earth's orbit plane, ( $O_x$ ) points toward the Sun, and ( $O_z$ ) points upward (coordinates (0°N, 0°E) correspond to encounters along the Sun-Earth vector). A Mollweide projection is used.

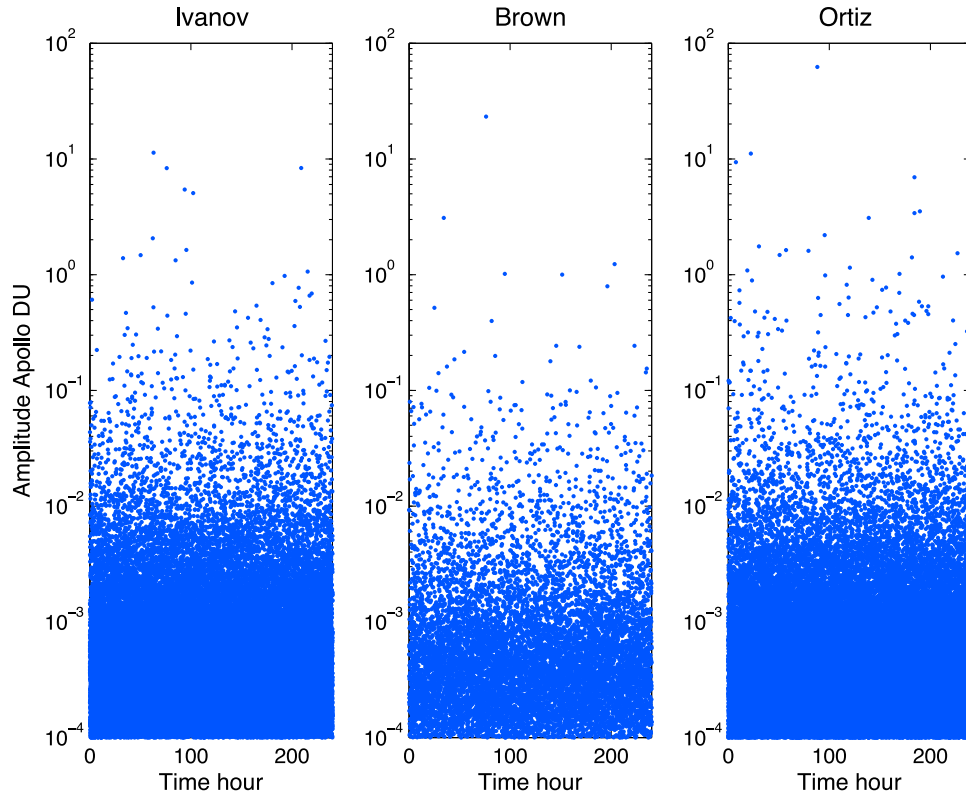


**Figure 14.** Simulated impact amplitudes. Each point provides the maximum envelope amplitude of a single simulated impact “recorded” at the station 12 location. From left to right are the simulations for the Ivanov, Brown, and Ortiz models, respectively. Each simulation spans 10 days.

shows that about 10% of the impacts have velocities below 10 km/s and about 90% below 30 km/s.

[42] In order to ensure that the Yarkovsky effect does not invalidate our model for the small masses considered in this study, we calculate the radiant distribution of bolides impacting the Earth in our simulation, and compare it to the radar observations of meteors described by *Campbell-Brown* [2008]. The distribution is defined as the direction of arrival of projectiles before any gravitational perturbations of the planet. In other words, the distribution is given by the direction of the vector  $\mathbf{v}$  defined above. Denoting  $\theta_r$  and  $\phi_r$  the spherical angles in the  $O_{xyz}$  coordinate system, corresponding to the colatitude and longitude, the velocity components are geometrically defined by  $v_x$ ,  $v_y$  and  $v_z$ . Providing that  $v_x = \pm\sqrt{v_x^2}$  and  $v_z = \pm\sqrt{v_z^2}$  with an equal probability due to the symmetry of the problem [Opik, 1951; Zahnle et al., 2001], we show the impact probability distribution in Figure 13. Note that Figure 13 is in excellent agreement with Figure 4 of *Campbell-Brown* [2008]. As radar can detect meteors of millimetric sizes, we consider that meteoroids reproduce the orbital behavior of larger objects, and that the model is well adapted for our purpose.

[43] For the impact mass and frequencies, we first use the model of *Brown et al.* [2002], providing the flux of small NEOs (diameter  $d \sim 1-10$  m) on the Earth. The flux of objects larger than a few cm scale follows a simple power law in agreement with estimates from *Halliday et al.* [1996] and *Harris* [2002] for diameter ranges  $d \sim 0.05-0.2$  m and  $d \sim 30-100$  m, respectively. Using our calculated Earth/Moon

impact rate ratio, the number of lunar impacts per year for masses larger than  $m$  is of the form

$$F(> m) = F_0 m^{-f} \quad (24)$$

where  $m$  is expressed in kg,  $F_0 = 1.29 \times 10^3$  and  $f = 0.90$ . We extrapolate this power law to masses as low as 1 g.

[44] For impact locations, we assume here that the flux is isotropic, which leads to a uniform probability of impact anywhere on the Moon. By doing so, we neglect spatial variations of the impact rate, that are estimated to be on the order of 25% [Zahnle et al., 2001; Morota and Furumoto, 2003; Le Feuvre and Wieczorek, 2008]. The isotropy assumption, following *Pierazzo and Melosh* [2000], implies that an impact with a given vertical impact angle  $\psi_v$  with respect to the normal to the surface (i.e., same definition as in section 3.1) has a probability proportional to  $\sin 2\psi_v$ . The tangential impact angle,  $\psi_h$ , defined as the angle between the impact velocity vector projected onto the surface and an arbitrary direction (for instance, East), is uniformly distributed, with a probability of  $1/2\pi$ . With these two angles, the three components of the impact velocity at the impact site are easily expressed in a spherical coordinate system  $(r, \theta, \phi)$ , and we can generate random impact conditions on the lunar surface for a given time period  $\delta t$ . Sampling of a given variable is performed by associating its normalized cumulative probability distribution with a uniform random number,

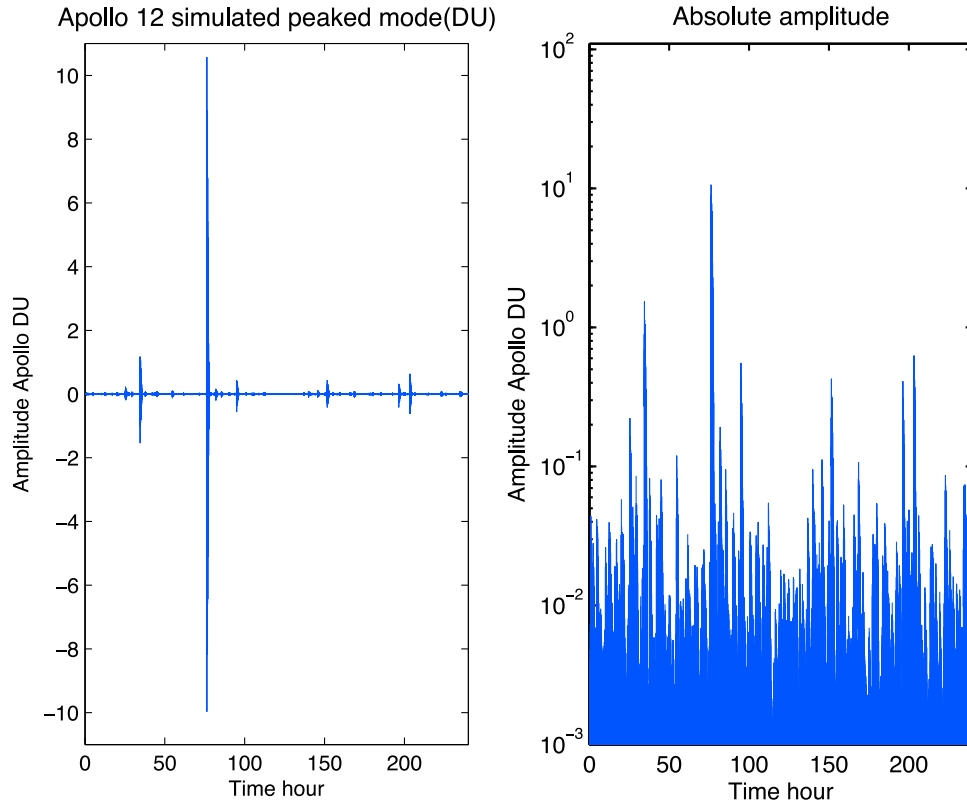


**Figure 15.** Composite waveform for impacts simulated using the Brown model. The duration of each waveform (corresponding to an individual impact) summed is 1 h, while the plot shows 10 days of signal. (left) The computed seismogram in Apollo DU. (right) The absolute value of the seismogram, on a logarithmic scale.

$x_i \in [0, 1]$ . Hence, each random impact is characterized by seven random numbers:

$$\begin{cases} u &= P_{<u}^{-1}(x_1) \quad m = m_0 x_2^{-1/f} \\ \theta &= \cos^{-1}(2x_3 - 1) \quad \phi = 2\pi x_4 \\ \psi_v &= \frac{1}{2} \cos^{-1}(2x_5 - 1) \quad \psi_h = 2\pi x_6 \\ t &= \Delta t x_7 \end{cases} \quad (25)$$

where  $\theta$  and  $\phi$  are the colatitude and longitude of the impact,  $\psi_v$  and  $\psi_h$  the vertical and horizontal angles of the impact,  $m$  and  $u$  the mass and velocity of the impactors, and  $t$  is the impact time.

[45] This approach provides a statistical model for the mass and velocity of impactors but however reveals little about their density. The jovian tisserand parameter, expressed as

$$T_j = \frac{a_j}{a} + 2\sqrt{(1-e^2)\frac{a}{a_j}} \cos i \quad (26)$$

where the subscript  $j$  refers to Jupiter's orbital elements, is usually used to discriminate dynamically between comets and asteroids. Although some overlap exists, it is generally considered that asteroids have  $T_j > 3$ , while nearly isotropic comets (including long-period comets and Halley-type comets) have  $T_j < 2$  [Bottke et al., 2002]. Jupiter family comets, that may be dormant or extinct, are dynamically linked to the giant planet, and have  $2 < T_j < 3$ . In our sim-

ulations, Jupiter family comets contribute only 14% to the lunar bombardment, with a mean impact velocity of about 26 km/s. Nearly isotropic comets [Dones et al., 2004] are not accounted for in the NEO model that is used here, but recent studies consider that they contribute by less than 10% to the overall bombardment [Weissman et al., 2002; Bottke et al., 2002]. Strokes et al. [2003] give an even lower estimate of 1%. Thus we use a fixed impactor density of  $3000 \text{ kg m}^{-3}$ . Equation (11) and Table 1 show that this assumption for the Jupiter family comets overestimates the amplitude of the seismic impulses by about 5%. The missing nearly isotropic comets probably underestimate the seismic hum by about 10%, and both simplifications have a net effect of less than 10%.

[46] We have performed these simulations for three impact/frequency models. The first two are Ivanov [2006] and Brown et al. [2002], while the third has the same slope as the Ivanov [2006] power law, but is normalized with the rate at 1 kg given by Ortiz et al. [2006] for masses larger than 1 kg; this rate is larger by about a factor of 3 than that derived from the Brown et al. [2002] model. Note that about 4000 objects of more than 1 kg impact the Moon per year. The three models will be referred to in the following as the Brown, Ivanov, and Ortiz models respectively.

## 5. Results and Discussion

[47] Using the method described above, we obtain a time series of impacts, with the position, time, vector velocity, and

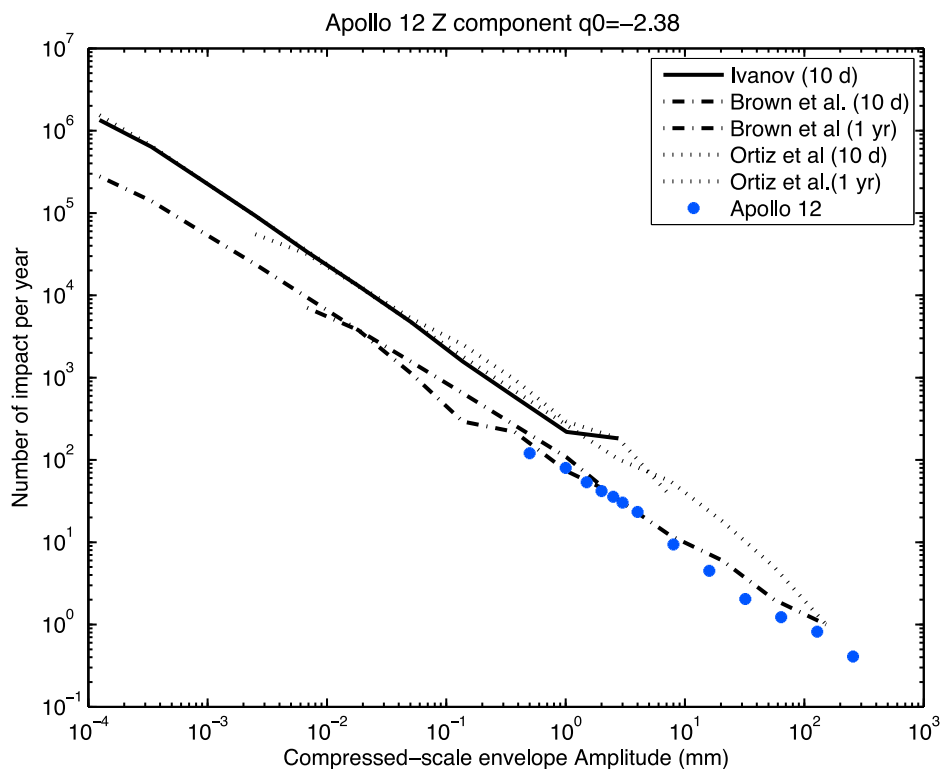


**Figure 16.** Number of impacts per year with a given amplitude modeled at station 12 using impact statistics derived from the Ivanov (solid line), Ortiz (dotted line), and Brown (dashed-dotted line) models. For comparison with the Apollo catalog information (circles), we report the compressed-scale envelope amplitude estimated from our synthetics. For the Brown and Ortiz impact models, the line segment on the left is for the 10 day simulation and corresponds to small impacts while the one on the right is for the 1 year simulation, corresponding to large impacts.

mass of each impactor. Each of these impacts generates a seismic signal, which we model following the method described in section 3.3, and add to a composite time series recorded at a given location. We choose here the Apollo 12 landing site: the sensitivity to the seismic station location will be discussed in the following section.

[48] Figure 14 shows the maximum amplitudes ( $A_{\max}$ ) for impacts occurring over 10 days, for the three different meteoroid models. The Ivanov and Ortiz models typically generate higher-amplitude signals than those of Brown, due to the greater impact frequencies for the same impactor mass. Figure 15 shows a typical modeled waveform, when we use the Brown model for the impact statistics. As described earlier, this waveform is obtained via the summation of all the waveforms associated with the modeled impacts, with each waveform scaled by the factor for its envelope maximum amplitude (equation (17)) and interpolated from the Apollo artificial impact seismograms following equations (20) and (21).

[49] The last step is the comparison of the statistics of our synthetic seismograms to those of Nakamura’s catalog (as the latter was formed by visual interpretation of data plotted on paper records). In order to check that our computation of the compressed-scale envelope amplitude from the Apollo digital data was correct, we again use the artificial impacts. We found amplitudes typically 20% larger than the cataloged amplitudes. For some large signals however, such as the impact of the Apollo 17 SIVB, the compressed-scale ampli-

tude in the catalog can be saturated, while the data are not (Y. Nakamura, personal communication, 2008). Compressed-scale amplitudes (in mm) are moreover found to be comparable to the maximum amplitudes of the signals (in DU), within  $\pm 15\%$ .

[50] To obtain a distribution of the number of impacts per year with a given amplitude, we computed the amplitudes of our impact synthetics at the Apollo 12 station following equation (17) (Figure 16). For the Brown and Ortiz impact models we included two trials: the first corresponds to a 10 day history of small impactors (mass in the range 1 g–500 kg). The second corresponds to a 1 year history of large impacts (masses in the range 5 g–5000 kg), comparable to those detected by Apollo. The upper mass limit depends on the duration of the trial. For the 10 day trial, we found maximum impactor masses of 85 kg, 128 kg and 516 kg for the Ivanov, Brown, and Ortiz models, with 11, 2, and 10 impactors having masses larger than 10 kg, respectively. For the 1 year trial, we found maximum masses of 8235 kg, and 2628 kg for the Brown and Ortiz models, with 155, and 412 impactors having masses larger than 500 kg, respectively (a 1 year trial was not conducted in the Ivanov study). Impacts simulated with the Brown model overlap fairly well with the observations and are extended toward much smaller amplitudes, with the same logarithmic slope. Impacts simulated with the Ivanov or Ortiz models are typically about a factor of 3.5 too large, in terms of frequency for a given mass (or about the same factor of 3.5, in terms of amplitude).

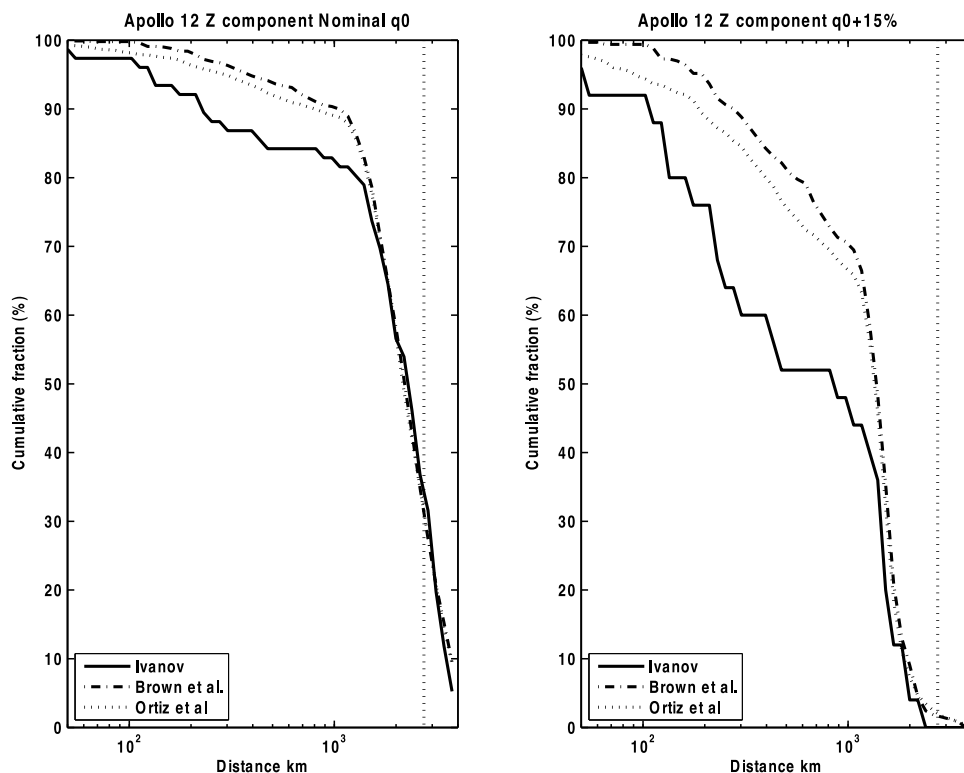


**Figure 17.** Cumulative percentage of impacts at a given epicentral distance for the (left) nominal and (right) high attenuation models. In the first case, about 30% of the events are found at epicentral distances greater than 90°, while this fraction is reduced to only a few percent in the high attenuation case. The high attenuation model reduces the amplitudes by a factor of up to 10 at epicentral distances of 2500 km (82°) and by 20 at 4000 km (132°).

[51] We note that many of the impacts in our simulation occur on the farside of the Moon, and that limited seismic observations of impacts were made at such large epicentral distances from the nearside Apollo array. Very few impacts were located at epicentral distances more than 120° [see Lognonné, 2005, Figure 2]. In contrast, our model predicts that about 30% of the impacts are detected at epicentral distances larger than 90° (Figure 17). We explored how the amplitudes of impacts at large epicentral distances are sensitive to the attenuation parameter  $q$ , especially for impacts recorded at epicentral distances greater than 50°. We find that a value for  $q_0$  increased by 15% provides a reasonable match to the observations for the Ivanov and Ortiz models (Figure 18), while the Brown model with this increased  $q_0$  predicts amplitudes that are too low for a given impact frequency. In terms of the quality factor  $Q$ , which is a more classical parameter than  $q$  for dealing with attenuation, we assume that

$$q^{\omega t} = e^{-\frac{\omega t}{2Q}} \quad (27)$$

where  $\omega_0$  is the central angular frequency of the signal and  $k$  is a constant. A change from  $q$  to  $q'$  is therefore equivalent to a change of the quality factor from  $Q$  to  $Q'$ :

$$\frac{\ln(q)}{\ln(q')} = 10^{-(q_0 - q'_0)} = \frac{Q'}{Q} \quad (28)$$

An increase of  $q_0$  by 15% is therefore associated with a division of the attenuation quality factor by a factor 2.46. This is comparable to the ratio of the shear quality factor in the upper mantle (about 1500) [Nakamura *et al.*, 1976] over the value in the lower mantle (about 500) [Toksoz *et al.*, 1974]. Even though models for the attenuation of the Moon's deep interior are far from definitive, we posit that the frequencies of impactors proposed by Ivanov and Ortiz provide a better match to the lunar seismic observations than those of Brown. More detailed analyses require an updated model of the lunar attenuation.

[52] We estimate the background seismic noise associated with meteoroid impacts by assuming that the amplitude observations made down to about 0.1 mm (compressed scale) by Apollo can be extrapolated to lower amplitudes due to the linearity of the seismic waves with respect to the impact impulse in the LP bandwidth (i.e., below 1 Hz). Extrapolation to higher frequencies requires better knowledge of the details of the high-frequency cutoff associated with impacts; this could lead to a saturation of the seismic amplitudes at high frequency. Such knowledge will of course request more sensitive instruments with better resolution and with Digital Units (DU) values smaller than those of the Apollo seismometers in terms of ground acceleration or displacement.

[53] Either the Brown model, or the Ivanov or Ortiz models with a larger and more realistic attenuation in the lower mantle, provide similar impact distributions and resulting background noise. Within the typical duration of a seismogram associated with a single lunar event (about 1 h), our

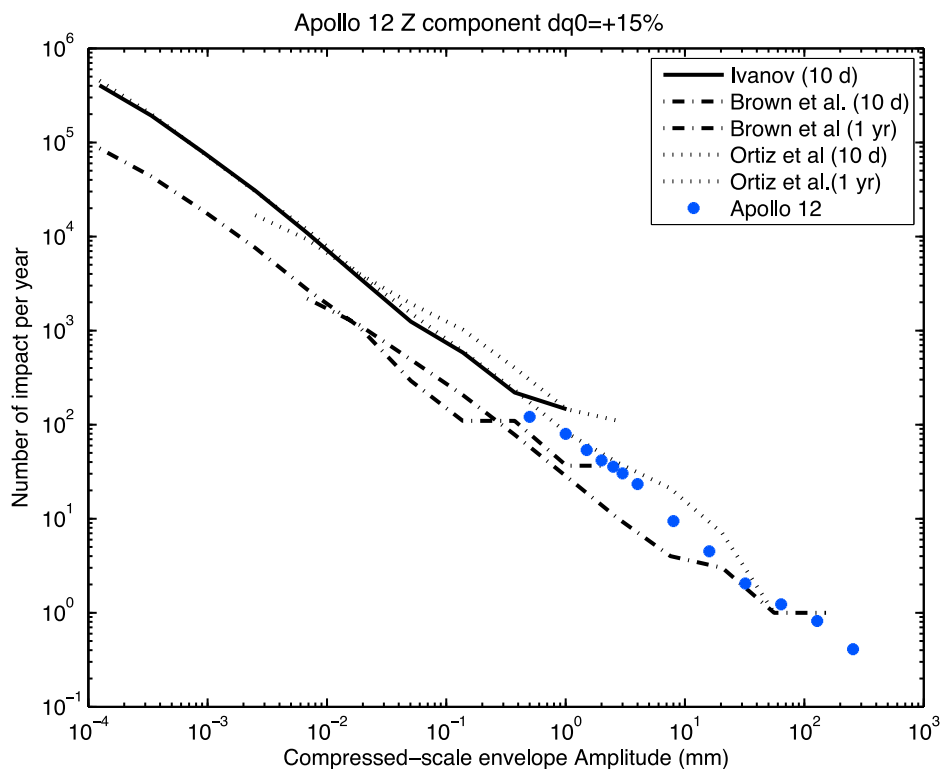


**Figure 18.** Number of impacts per year with a given amplitude modeled at station 12 using impact statistics derived from the Ivanov, Brown, and Ortiz models, with  $q_0$  greater by 15% in the Ivanov and Ortiz models. This is equivalent to a decrease of the seismic quality factor by about  $10^{2.56 \times 0.15} = 2.42$ . Conventions are the same as for Figure 16.

model predicts several impacts with amplitudes of  $10^{-2}$  DU (where one DU is the Apollo sensitivity, about  $0.5 \times 10^{-10}$  m in ground displacement at 2 sec), and several with amplitudes an order of magnitude smaller. This generates a background noise with maximum amplitudes fluctuating between  $10^{-3}$  and  $10^{-2}$  DU. Several events per day peak above this noise background, and have amplitudes from a few tenths of a DU to several DU. The detection of this permanent signal will permit high-resolution and systematic crustal studies, as already initiated by *Vinnik et al.* [2001] and will, therefore, request resolutions  $10^2$  to  $10^3$  better than Apollo.

[54] Deep moonquakes will also contribute to the background noise, possibly periodically due to the nature of deep moonquake occurrence shown in Figure 4 and discussed in the introduction. Individual deep moonquake signals can be detected by cross-correlation techniques [e.g., *Lognonné and Johnson, 2007*] and therefore “subtracted” from the signal by signal processing. Even if such techniques are necessary in order to detect several overlapping small moonquakes, we think that the impact-generated noise will be the ultimate noise found on the data, either during quiet deep moonquake periods, or after data processing and deep moonquake extraction. This noise will also be a limiting factor, in addition to the instrument noise, in the stacks of deep moonquakes.

[55] In conclusion, we find a mean RMS noise (in one minute duration windows) below  $1.5 \times 10^{-3}$  DU about 50% of the time and below  $10^{-2}$  DU 90% of the time. In terms of peak-to-peak amplitudes, this leads to peak-to-peak amplitudes below  $0.75 \times 10^{-2}$  DU 50% of the time and 0.045 DU about 90% of the time, for the same one minute duration

window. This latter value might be considered a robust detection threshold for single impact events by VBB seismometers [*Lognonné et al., 2000; Lognonné, 2005*], and can be used for future lunar seismic experiment design, such as that under consideration for the International Lunar Network. An RMS noise level of 0.01 DU corresponds to  $0.5 \times 10^{-11}$  m/s<sup>2</sup> in acceleration at periods of 2 s and about  $1.5 \times 10^{-11}$  m/s<sup>2</sup> peak-to-peak. We note also that many events per day peak with amplitudes larger than 0.1 DU. Extrapolation to longer periods, if the noise is mainly related to impacts, suggests that at a period of 20 s (corresponding to long-period body waves or crustal surface waves) we can expect a noise level one thousand times smaller in acceleration (10 times smaller in displacement), while a decrease of only one hundred is obtained on the Earth. However, the modeling of the long-period noise must integrate the surface wave noise, which is excited by impacts with high incidence angles, but not considered in this work. Nevertheless, a noise level smaller than  $10^{-3}$  of the Earth low noise model value is very likely. This very low noise level, probably below the detection threshold of VBBs and detectable only with superconducting instruments, might also be compatible with detecting the passage of  $\sim 1$  gram nuggets of strange quark matter [*Banerdt et al., 2006*]. Future VBB seismometers, such as those proposed for SELENE2 [*Tanaka et al., 2008*] or the International Lunar Network [*Weinberg et al., 2008; Banerdt and Lognonné, 2008*] might then be able to detect not only several thousands of impacts per year, but also possibly these type of particles.

## 6. Conclusions

[56] We have developed an empirical approach for generating synthetic seismograms representing the continuous flux of meteorite impacts on the Moon. Our approach takes into consideration the following source effects: impactor incidence angle, mass, speed, the production of ejecta, radiation patterns for P and S waves, and seismic ray incidence angle at the receiver. The dependence of amplitude on epicentral distance integrates the effects of attenuation and diffraction. We use these effects to calibrate the maximum amplitudes of artificial impacts recorded on the vertical long-period channel at station 12.

[57] The meteoroid flux on the moon is modeled using the NEO model of *Bottke et al.* [2002], with impact masses and frequencies described by three models [*Brown et al.*, 2002; *Ivanov*, 2006; *Ortiz et al.*, 2006]. For a given meteoroid impact (known location, speed, impact angle and mass) we use seismograms from the two closest artificial impacts together with our amplitude calibration to produce an empirical waveform for our meteoroid seismic source. We compute composite seismograms for impact histories spanning 10 day and 1 year time intervals.

[58] Our results suggest that the Apollo observed impact detection rate and amplitude statistics are well matched by the *Ivanov* [2006] and *Ortiz et al.* [2006] models if the increase of lunar attenuation with depth is incorporated in the models. A meteoritic background noise level with peak-to-peak amplitudes smaller than  $2 \times 10^{-11}$  m/s<sup>2</sup> is predicted, at least 1000 times lower than the Earth low noise model, and several impacts per day peak above this background noise. These results must be taken into account in the design of future lunar seismometers. Finally, we note that the model formulation here is general and can be further tested and calibrated using future observations, in particular future artificial impacts recorded by new lunar seismic stations.

[59] **Acknowledgments.** P. Lognonné thanks the Department of Earth and Ocean Sciences, UBC, Vancouver for hosting a visit in summer 2007 and 2009, during which time this research was initiated and finalized. C. Johnson acknowledges support from NASA Planetary Geology and Geophysics grant NNX08AL49G and NSERC. We thank W. Bottke and A. Morbidelli for having shared their model. We thank Mark Wieczorek for useful comments, Y. Nakamura for very fruitful discussions, as well as an anonymous reviewer. This work was supported by PNP and CNES. This is IGP contribution 2540.

## References

- Aki, K. (1992), Scattering conversions P to S versus S to P, *Bull. Seismol. Soc. Am.*, *82*, 1969–1972.
- Aki, K., and P. G. Richards (2002), *Quantitative Seismology*, 2nd ed., University Sci. Books, Sausalito, Calif.
- Ball, A. J., P. Lognonné, K. Seiferlin, M. Pätzold, and T. Spohn (2004), Lander and penetrator science for near-Earth object mitigation studies, in *Mitigation of Hazardous Impacts due to Asteroids and Comets*, edited by M. J. S. Belton et al., pp. 266–291, Cambridge Univ. Press, New York.
- Banerdt, W. B., and P. Lognonné (2008), ALGEP: An autonomous lunar geophysical experiment package, *Lunar Planet. Sci.*, XXXIX, Abstract 2228.
- Banerdt, W. B., T. Chui, E. T. Herrin, D. Rosenbaum, and V. L. Teplitz (2006), Lunar seismic search for strange quark matter, *Adv. Space Res.*, *37*, 1889–1893, doi:10.1016/j.asr.2005.06.034.
- Bottke, W. F., A. Morbidelli, R. Jedicke, J.-M. Petit, H. F. Levison, P. Michel, and T. S. Metcalfe (2002), Debaised orbital and absolute magnitude distribution of the near-Earth objects, *Icarus*, *156*, 399–433.
- Brown, P., R. E. Spalding, D. O. ReVelle, E. Tagliaferri, and S. P. Worden (2002), The flux of small near-Earth objects colliding with the Earth, *Nature*, *420*, 294–296.
- Bulow, R. C., C. L. Johnson, and P. M. Shearer (2005), New events discovered in the Apollo lunar seismic data, *J. Geophys. Res.*, *110*, E10003, doi:10.1029/2005JE002414.
- Campbell-Brown, M. D. (2008), High resolution radiant distribution and orbits of sporadic radar meteoroids, *Icarus*, *196*, 144–163.
- Carrier, W. D., III, G. R. Olhoeft, and W. Mendell (1991), Physical properties of the lunar surface, in *Lunar Sourcebook, A User's Guide to the Moon*, edited by G. H. Heiken et al., section 9, pp. 475–594, Cambridge Univ. Press, Cambridge, U. K.
- Chenet, H., P. Lognonné, M. Wieczorek, and H. Mizutani (2006), Lateral variations of lunar crustal thickness from the Apollo seismic data set, *Earth Planet. Sci. Lett.*, *243*, 1–2.
- Dainty, A. M., and M. N. Toksoz (1977), Elastic wave propagation in a highly scattering medium: A diffusion approach, *J. Geophys.*, *43*, 375–388.
- Dainty, A. M., M. N. Toksoz, K. R. Anderson, P. J. Pines, Y. Nakamura, and G. Latham (1974), Seismic scattering and shallow structure of the Moon in Oceanus Procellarum, *Moon*, *9*, 11–29.
- Dones, L., P. R. Weissman, H. F. Levison, and M. J. Duncan (2004), Oort cloud formation and dynamics, in *Star Formation in the Interstellar Medium: In Honor of David Hollenbach, Chris McKee, and Frank Shu*, *Astron. Soc. of the Pac. Conf. Ser.*, vol. 323, pp. , 371–384, San Francisco, Calif.
- Edwards, D. L., W. Cooke, D. E. Moser, and W. Swift (2008), Measurement of ejecta from normal incident hypervelocity impact on lunar regolith simulant, *Earth Moon Planets*, *102*, 549–553.
- Evans, J. R. (1982), Running median filters and a general despiker, *Bull. Seismol. Soc. Am.*, *72*, 331–338.
- Ewing, M., G. Latham, F. Press, G. Sutton, J. Dorman, Y. Nakamura, R. Meissner, F. Duennebier, and R. Kovach (1971), Seismology of the Moon and implications on internal structure, origin and evolution, in *Highlights of Astronomy*, pp. 155–172, D. Reidel, Dordrecht, Netherlands.
- Frohlich, C., and Y. Nakamura (2009), The physical mechanisms of deep moonquakes and intermediate-depth earthquakes: How similar and how different?, *Phys. Earth Planet. Inter.*, *173*, 365–374.
- Gagnepain-Beyneix, J., P. Lognonné, H. Chenet, D. Lombardi, and T. Spohn (2006), A seismic model of the lunar mantle and constraints on temperature and mineralogy, *Phys. Earth Planet. Inter.*, *159*, 140–166.
- Gupta, I. N. (1966), Body wave radiation patterns from force applied within a half-space, *Bull. Seismol. Soc. Am.*, *56*, 173–183.
- Halliday, I., A. A. Griffin, and A. T. Blackwell (1996), Detailed data for 259 fireballs from the Canadian camera network and inferences concerning the influx of large meteoroids, *Meteorit. Planet. Sci.*, *31*, 185–217.
- Harris, A. W. (2002), A new estimate of the population of small neas, *Bull. Seismol. Soc. Am.*, *34*, 835.
- Holsapple, K. A. (1993), The scaling of impact processes in planetary sciences, *Annu. Rev. Earth Planet. Sci.*, *21*, 333–373.
- Holsapple, K. A. (2004), About deflecting asteroids and comets, in *Mitigation of Hazardous Comets and Asteroids*, edited by M. J. S. Belton et al., pp. 113–140, Cambridge Univ. Press, Cambridge, U. K.
- Holsapple, K. A., and K. R. Housen (2007), A crater and its ejecta: An interpretation of deep impact, *Icarus*, *191*, 586–597.
- Housen, K. R., R. M. Schmidt, and K. A. Holsapple (1983), Crater ejecta scaling laws: Fundamental forms based on dimensional analysis, *J. Geophys. Res.*, *88*, 2485–2499.
- Ingersoll, A. P., H. Kanamori, and T. E. Dowling (1994), Atmospheric gravity waves from the impact of comet Shoemaker-Levy 9 with Jupiter, *Geophys. Res. Lett.*, *21*, 1083–1086.
- Ivanov, B. A. (2006), Cratering rate comparisons between terrestrial planets, in *Workshop on Surface Ages and Histories: Issues in Planetary Chronology*, *LPI Contrib.*, *1320*, 26–27.
- Kobayashi, N., and K. Nishida (1998), Continuous excitation of planetary free oscillations by atmospheric disturbances, *Nature*, *395*, 357–360.
- Kovach, R., J. S. Watkins, and P. Talwani (1973), *Apollo 17: Preliminary Science Report*, *NASA SP-330*, chap. Lunar Seismic Profiling Experiment, pp. , 10.1–10.12.
- Lammlin, D. R., G. V. Latham, J. Dorman, Y. Nakamura, and M. Ewing (1974), Lunar seismicity, structure, and tectonics, *Rev. Geophys.*, *12*, 1–21.
- Larose, E., A. Khan, Y. Nakamura, and M. Campillo (2005), Lunar subsurface investigated from correlation of seismic noise, *Geophys. Res. Lett.*, *32*, L16201, doi:10.1029/2005GL023518.
- Laster, S. J., and F. Press (1968), A new estimate of lunar seismicity due to meteorite impact, *Phys. Earth Planet. Inter.*, *1*, 151–154.
- Latham, G. V., W. G. McDonald, and H. J. Moore (1970a), Missile impacts as sources of seismic energy on the Moon, *Science*, *168*, 242–245.
- Latham, G. V., et al. (1970b), Passive seismic experiment, *Science*, *167*, 455–457.
- Latham, G., M. Ewing, J. Dorman, D. Lammlin, F. Press, N. Toksoz, G. Sutton, F. Duennebier, and Y. Nakamura (1971), Moonquakes, *Science*, *174*, 687–692.

- Le Feuvre, M., and M. A. Wieczorek (2008), Nonuniform cratering of the terrestrial planets, *Icarus*, *197*, 291–306.
- Lognonné, P. (2005), Planetary seismology, *Annu. Rev. Earth Planet. Sci.*, *33*, 571–604.
- Lognonné, P., and C. L. Johnson (2007), Planetary seismology, *Treatise Geophys.*, *10*, pp. 69–122, doi:10.1016/B978-044452748-6.00154-1.
- Lognonné, P., and B. Mosser (1993), Planetary seismology, *Surv. Geophys.*, *14*, 239–302.
- Lognonné, P., B. Mosser, and F. A. Dahlen (1994), Excitation of Jovian seismic waves by the Shoemaker-Levy 9 cometary impact, *Icarus*, *110*, 180–195.
- Lognonné, P., et al. (2000), The NetLander very broad band seismometer, *Planet. Space Sci.*, *48*, 1289–1302.
- Lognonné, P., G. Gagnepain-Beyneix, and H. Chenet (2003), A new seismic model of the Moon: Implications for structure, thermal evolution and formation of the Moon, *Earth Planet. Sci. Lett.*, *211*, 27–44.
- McGarr, A., G. V. Latham, and D. E. Gault (1969), Meteoroid impacts as sources of seismicity on the Moon, *J. Geophys. Res.*, *74*, 5981–5994.
- Morota, T., and M. Furumoto (2003), Asymmetrical distribution of rayed craters on the Moon, *Earth Planet. Sci. Lett.*, *206*, 315–323.
- Nakamura, Y. (1976), Seismic energy transmission in the lunar surface zone determined from signals generated by movement of lunar rovers, *Bull. Seismol. Soc. Am.*, *66*, 593–606.
- Nakamura, Y. (1977), Seismic energy transmission in an intensively scattering environment, *J. Geophys.*, *43*, 389–399.
- Nakamura, Y., F. K. Duennebier, G. V. Latham, and H. J. Dorman (1976), Structure of the lunar mantle, *J. Geophys. Res.*, *81*, 4818–4824.
- Nakamura, Y., G. V. Latham, and H. J. Dorman (1980), How we processed Apollo lunar seismic data, *Phys. Earth Planet. Inter.*, *21*, 218–224.
- Nakamura, Y., G. V. Latham, H. J. Dorman, and J. E. Harris (1981), Passive seismic experiment long period event catalog, *Tech. Rep. 118*, Inst. for Geophys., Univ. of Tex., Austin.
- Oberst, J., and Y. Nakamura (1987a), Lunar seismic impact clusters: Evidence for the presence of “meteorite streams”, *Lunar Planet. Sci.*, *XVIII*, Abstract 736.
- Oberst, J., and Y. Nakamura (1987b), Distinct meteoroid families identified on the lunar seismograms, *J. Geophys. Res.*, *92*, 769–773.
- Oberst, J., and Y. Nakamura (1991), A search for clustering among the meteoroid impacts detected by the Apollo lunar seismic network, *Icarus*, *91*, 315–325.
- Opik, E. J. (1951), Collision probability with the planets and the distribution of planetary matter, *Proc. R. Irish Acad. Sect. A*, *54*, 165–199.
- Ortiz, J. L., et al. (2006), Detection of sporadic impact flashes on the Moon: Implications for the luminous efficiency of hypervelocity impacts and derived terrestrial impact rates, *Icarus*, *184*, 319–326.
- Papanicolaou, G. C., L. V. Ryzhik, and J. B. Keller (1996), Stability of the P-to-S energy ratio in the diffusive regime, *Bull. Seismol. Soc. Am.*, *86*, 1107–1115.
- Pierazzo, E., and H. J. Melosh (2000), Understanding oblique impacts from experiments, observations, and modeling, *Annu. Rev. Earth Planet. Sci.*, *28*, 141–167.
- Richardson, J. E., H. J. Melosh, R. J. Greenberg, and D. P. O’Brien (2005), The global effects of impact-induced seismic activity on fractured asteroid surface morphology, *Icarus*, *179*, 325–349.
- Shapiro, N. M., and M. Campillo (2004), Emergence of broadband Rayleigh waves from correlations of the ambient seismic noise, *Geophys. Res. Lett.*, *31*, L07614, doi:10.1029/2004GL019491.
- Shapiro, N. M., M. Campillo, L. Stehly, and M. H. Ritzwoller (2005), High-resolution surface-wave tomography from ambient seismic noise, *Science*, *307*, 1615–1618.
- Strobach, K. (1970), Scattering of seismic waves and lunar seismograms, *J. Geophys.*, *36*, 643–645.
- Strokes, G. H., et al. (2003), Study to determine the feasibility of extending the search for near-Earth objects to smaller limiting diameters, *Rep. of the Near-Earth Science Definition Team*, NASA Off. of Space Sci., Washington, D. C.
- Stuart, J. S., and R. P. Binzel (2004), Bias-corrected population, size distribution, and impact hazard for the near-Earth objects, *Icarus*, *170*, 295–311.
- Tanaka, S., H. Shiraishi, M. Kato, T. Okada, and Science Working Group of Post SELENE Missions (2008), The science objectives of the SELENE-II mission as the post SELENE mission, *Adv. Space Res.*, *42*, 394–401.
- Tanimoto, T., M. Eitzel, and Y. Tomoko (2008), The noise cross-correlation approach for Apollo 17 LSPE data: Diurnal change in seismic parameters in shallow lunar crust, *J. Geophys. Res.*, *113*, E08011, doi:10.1029/2007JE003016.
- Toksoz, M. N., A. M. Dainty, S. C. Solomon, and K. R. Anderson (1974), Structure of the Moon, *Rev. Geophys.*, *12*, 539–567.
- Toksoz, M. N., N. R. Goins, and C. H. Cheng (1977), Moonquakes: Mechanisms and relation to tidal stresses, *Science*, *196*, 979–981.
- Vinnik, L., H. Chenet, J. Gagnepain-Beyneix, and P. Lognonné (2001), First seismic receiver functions on the Moon, *Geophys. Res. Lett.*, *28*, 3031–3034.
- Walker, J. D., and W. F. Huebner (2004), Seismological investigation of asteroid and comet interiors, in *Mitigation of Hazardous Comets and Asteroids*, edited by M. J. S. Belton et al., pp. 234–265, Cambridge Univ. Press, Cambridge, U. K.
- Webb, S. C. (2008), The Earth’s hum: The excitation of Earth normal modes by ocean waves, *Geophys. J. Int.*, *174*, 542–566.
- Weinberg, J. D., C. R. Neal, P. Lognonné, L. L. Hood, and S. Huang (2008), Lunar Geophysical Instrument Package (LGIP) I: Science and instrumentation, *Lunar Planet. Sci.*, *XXXIX*, Abstract 1433.
- Weissman, P. R., W. F. Bottke, and H. F. Levison (2002), Evolution of comets into asteroids, in *Asteroids III*, edited by W. F. Bottke Jr., pp. 669–686, Univ. of Ariz. Press, Tucson.
- Yamamoto, S. (2002), Measurement of impact ejecta from regolith targets in oblique impacts, *Icarus*, *158*, 87–97.
- Zahnle, K., P. Schenk, S. Sobieszczyk, L. Dones, and H. F. Levison (2001), Differential cratering of synchronously rotating satellites by ecliptic comets, *Icarus*, *153*, 111–129.

C. L. Johnson, Department of Earth and Ocean Sciences, University of British Columbia, Vancouver, BC V6T 1Z4, Canada.

M. Le Feuvre and P. Lognonné, Equipe Géophysique Spatiale et Planétaire, UMR 7154, Institut de Physique du Globe de Paris, Université Paris Diderot, CNRS, 4 Ave. de Neptune, Saint Maur des Fosses F-94107, France. (lognonne@ipgp.jussieu.fr)

R. C. Weber, U.S. Geological Survey, 2255 North Gemini Dr., Flagstaff, AZ 86001, USA.